Developing a robust quantum simulator with trapped ions

by

Lewis Hahn

A thesis
presented to the University of Waterloo
in fulfilment of the
thesis requirement for the degree of
Master of Science
in
Physics (Quantum Information)

Waterloo, Ontario, Canada, 2024

© Lewis Hahn 2024

Author's Declaration

I hereby declare that I am the sole author of this thesis. This is a true copy of the thesis, including any required final revisions, as accepted by my examiners.

I understand that my thesis may be made electronically available to the public.

Abstract

Trapped ion systems have experienced significant growth in recent years as their potential for excelling as quantum simulators has become recognized. Ions make an excellent qubit due to their long coherence times with moderate gate times, high fidelity detection and state initialization, and their ability to create long range spin interactions. As the experimental demands of trapped ions increases, so too do the demands that sustain and control them. In this thesis, I will cover the design and implementation of robust systems for the trapped ions platform and describe the development of robust lab infrastructure, equipment, and optics required to perform high contrast entangling operations on an existing four-rod system. By redesigning the DC power distribution and grounding system I have been able to supply our quantum simulator with clean DC voltages while reducing ground loops that can introduce noise into the system. With delicate alignment of the 355 nm system, our four-rod system is able to entangle qubits together. By incorporating 3D printing and inexpensive DC motors, I was able to motorize the controls used to align our 355 nm beam in the vertical direction which has made alignment reliable and accessible. With future iterations of the motorized stage, I've been able to achieve a resolution of 70 nm in all three axes. We then look to the next generation ion trap in the form of a meticulously engineered blade trap. With the ability to perform simulations on systems of about 30 qubits, reaching very low vacuum pressures is essential to increase ion life times. By careful preparation of our Shapal blade holder I've been able to preserve the 9×10^{-13} mbar pressure of our blade trap vacuum chamber. I then discuss the design of the imaging system for the blade trap which utilizes dual 0.5 NA (numerical aperture) objectives to achieve high state detection fidelity ($\sim 99.9\%$). By simulating the imaging system and taking into consideration the effects of the systems' efficiencies, I find that high state detection fidelity should be achievable for detection times on the order of 20 μs. This offers potential for performing in-situ mid-circuit measurement on the blade trap system. By performing some initial tests, I compare the experimental results to the simulated performance of the imaging system and find they match reasonably well.

Acknowledgements

I would like to extend my deepest thanks to my supervisor, Dr. Rajibul Islam. I came to Rajibul as a second year undergrad looking to experience work in an experimental lab. He gave me the opportunity to volunteer with QITI lab and has provided support ever since. I will be forever grateful to Rajibul for the experience he has given me.

I would like to thank my advisory committee Dr. Thomas Jennewein and Dr. Raymond Laflamme for their guidance and for pushing me to be a better communicator of science.

I would like to thank my lab mates at QITI lab for whom I've had the honour to work with over the years. Sainath, Nikhil and Roland, have been amazing mentors throughout my masters and co-op terms. I am extremely grateful to Chung-You, Jingwen, Anthony, Yu-Ting, Shilpa, Sakshee, Siddharth and Fabien for being exceptional labmates.

Courses would have been much more challenging if it were not for Owen and Justin. I am grateful for the support you two have given me over the years.

I would also like to thank my parents for their support and encouragement throughout my education. Lastly, without the support of my partner, Katie, none of this would have been possible.

Dedication

This is dedicated to those who keep our mouths full.

Table of Contents

Author's Declaration **ii**

Abstract **iii**

Acknowledgements **iv**

Dedication **v**

List of Figures **viii**

List of Abbreviations **xvi**

1 Introduction **1**

1.1 Four-rod trap quantum simulator 3

1.2 Blade trap 5

1.3 Outline 6

2 Trapped ion physics **7**

2.1 Trapping and state preparation 7

2.2 Single qubit rotation 10

2.3 Entangling operations 12

2.4 Implementing Raman transitions 13

3 Designing robust systems **14**
3.1 History . . . 15
3.2 Lab infrastructure . . . 16
3.2.1 Environmental stability . . . 17
3.2.2 Power distribution and grounding . . . 19
3.3 Lasers and Optics . . . 23
3.3.1 355nm layout . . . 23
3.3.2 Mechanical stability, referencing and optical control . . . 27
3.3.3 Beam alignment . . . 29
3.3.4 Two-qubit entangling . . . 35
3.4 Reaching XHV . . . 36
3.5 Summary and Discussion . . . 38

4 Blade trap imaging **39**
4.1 State of the art . . . 40
4.2 Detection physics . . . 42
4.3 Optical layout . . . 45
4.4 Design requirements for mid-circuit measurement . . . 48
4.4.1 System efficiencies . . . 48
4.4.2 Attenuation of a classical beam . . . 49
4.4.3 Reaching high state detection fidelity . . . 51
4.5 Blending mechanical and optical engineering . . . 54
4.5.1 High NA mechanical engineering . . . 54
4.5.2 The art of optical engineering . . . 56
4.6 Doublet testing . . . 62
4.7 Summary and Discussion . . . 64

5 Conclusion **67**

References **70**

List of Figures

1.1 **Four-rod trap quantum simulator.** Near the center of a 5ft × 10ft optics tables sits a four-rod Paul trap (upper right) inside a vacuum chamber. Along the top shows a linear chain of 18 $^{171}Yb^{+}$ ions trapped in this apparatus. ECDL (not visible in the image) generate laser light which is prepared (bottom left) and delivered onto the ions to perform various operations like Doppler cooling and state detection. Light from a 355 nm pulsed laser (middle right) is split into two paths and brought to the ions to perform coherent operations. An imaging system (center back) collects photons emitted from the ions for state detection. 2

1.2 **Blade trap vacuum assembly and internals.** The top image shows the vacuum assembly for the blade trap. A front facing window and four re-entrant windows provide optical access to address and image the ion. Bottom left shows a side view of the segmented blade trap. Wires carry RF and DC voltages to confine and control the ion. The bottom center shows the front facing view of the blade trap. The gold coated segmented blades are positioned to give 0.5 NA optical access from the sides and 0.3 NA from the top and bottom and are held in place with the Shapal blade holder. . 4

2.1 **Internal energy level diagram of** $^{171}Yb^{+}$ [1]. The red text shows the primary transitions used in the 4-rod trap system. 8

2.2 $^{171}Yb^{+}$ **cooling and state initialization transitions.** The left shows the $^{2}S_{1/2}$ to $^{2}P_{1/2}$ transition used for Doppler cooling. The hyper-fine and Zeeman levels are not shown here for simplicity. The 369.5 nm laser is detuned from the $^{2}P_{1/2}$ states by $\delta = 30$ MHz in our four-rod trap. The right diagram includes the hyper-fine levels of the S and P manifold used for state initialization (optical pumping). A 369.5nm laser is tuned to the $|\uparrow\rangle$ ($|F = 1\rangle$ state) to $|F' = 1\rangle$ transition. Once in the excited state, the ion has an approximate 1/3 probability of decaying to the $|\downarrow\rangle$ ($|F = 0\rangle$) state. . 9

2.3 **Energy level diagram for driving stimulated Raman transitions.** Two laser frequencies from a 355 nm pulsed laser, ω_1 and ω_2 are detuned from the excited state, $|e\rangle$ by an amount $\Delta = 33$THz. Here $\omega = |\omega_1 - \omega_2|$ is the frequency difference between the two lasers, while $|e\rangle$ is the $^{2}P_{1/2}$ manifold in our four-rod trap. 10

2.4 **Mølmer-Sørensen level diagram.** Here, ω_m is the frequency of the m^{th} motional mode and μ is the lasers detuning, referred to as the MS detuning. Red and blue arrows indicate the symmetrical detunings of the RSB and BSB Raman transitions needed to drive flopping from $|\downarrow\downarrow\rangle$ to $|\uparrow\uparrow\rangle$. 12

3.1 **The optics table layout for B221A.** 8020 Aluminum extrusions are used for the enclosure surrounding the tables with aluminum sheets used for the corner supports and top plates. Five hepa filters on top will connect to the air handling unit while two stand-alone hepa fan units will work as a back up if the HVAC unit is not operational. Enclosure doors are left out for clarity 17

3.2 **Water cooled amplifier box.** Thermally conductive, electrically isolating mounting tape is used to mount eight MPA-40-40 amplifiers from RF Bay to a water cooling plate to provide heat removal while keeping the amplifiers floating w.r.t. the box ground. Heat sinks are attached to the plate for back up heat removal. The front cover of the 4U Hammond box uses a 3D printed plate to electrically isolate the box from the SMA connectors. 18

3.3 **DC power distribution.** Two layouts for the DC distribution system in QITI lab (B221B). Flexable Festoon cables (yellow) are used to bring DC voltages from power supplies to custom made distribution boards placed (bottom left) around the lab. The top left scheme follows a tree structure, where a single Festoon cable (trunk) is brought from high wattage power supply to the lab. Branches are then connected to the trunk and used to supply the distribution boards. The top right scheme uses individual power supplies for each distribution board, which requires the Festoon cable be run directly from the distribution board to the power supply (bottom right). 20

3.4 **DC power distribution spectrum measurement.** On the left is the test setup used to measure the frequency power spectrum of the DC power distribution to ensure the power supply switch frequency or any other noise is not transferred to the DC voltages. The power supply is connected to a distribution board using a 15 ft Festoon cable. A high power resistor is used to simulate lab conditions and loads. A 1× oscilloscope probe was connected to a battery powered spectrum analyzer (Keysight Technologies FieldFox N9937A, 5 kHz to 18 GHz) to measure the frequency spectrum. The spectrum measurement on the right was performed on the 24 V channel with a 20 Ω resistor. The x-axis spans frequencies from 5 kHz to 1 MHz. The y-axis measures the power in dBm contained in each frequency bandwidth (7.5 kHz). The spectrum shows that the linear regulators on the distribution board have properly suppressed the switching noise from the power supply and any other pickup from the long Festoon cable. 22

3.5 **Four-rod trap** 355 nm **optical design.** Optical design for 355 nm optics used to drive Raman transitions in the four-rod quantum simulator. The F = 250 mm cylindrical lens is placed to shrink the horizontal direction to achieve a 70 μm beam waist along the ion chain. A 5× beam expander (Edmund Optics) is paired with a F = 150 mm spherical lens to shrink the vertical beam waist to approximately 5 μm at the ions. 24

3.6 **Four-rod trap** 355 nm **optical schematic.** 355 nm light from a Paladin Advanced 355-8000 (8 W) has its intensity reduced before splitting into RP1 and RP2 using a high power Polarizing Beamsplitter Cube from Thorlabs. The beams pass through AOMs for amplitude, frequency, and phase control before being shaped by the optics that follow. The beams overlap on the ions in order to drive single qubit rotations and entangling operations. Trap electrical and mechanical connections are not shown. RP2 has a retro-reflector for path length matching to ensure that the pulse trains from each path meet at the ion simultaneously. Mirrors M1 and M2 are used to roughly match the 204(6) mm path lengths to within a few millimeters. Diagram not to scale. 26

3.7 **Optical stability and referencing.** Examples of optical stability and referencing in the 4-rod Raman system. Each element shown can be easily removed for initial alignment and is referenced to the center of the beam. Left: spherical lens (F = 150 mm) that focuses the beam on the ion. Center: cylindrical lens (F = 250 mm) on a rotation mount that creates the elliptical beam. Right: 5× beam expander rigidly mounted to a v-clamp. 27

3.8 **Motorized translation stage.** Left shows the first iteration of of the motorized translation stage. This was installed on the translation stage that adjusts the vertical position of the final lens of the 4-rod Raman setup. Right shows the revised version that gives approximately 70 nm of precision on all 3 axes by using small DC motors with an approximate gear ratio of 1000 : 1 (top right). 28

3.9 355 nm **beam image.** Top is the image of the RP2 355 nm beam at the ions captured using a FLIR camera (BFS-PGE-120S4M-CS) with a pixel size of 1.85 μm × 1.85 μm. Bottom is a Gaussian fit of the image and gives a beam waist of 3 μm in the vertical direction and 65 μm along the horizontal. Linear colour scale indicates the irradiance of the beam (arbitrary units). . 29

3.10 355 nm **alignment using off-resonant microwave Ramsey interferometry.** Top shows the experimental sequence of a Microwave Ramsey experiment. The energy level diagrams show how applying 355 nm during the wait time (t) light has the effect of increasing the effective detuning (δ') of the microwave frequency from the qubit frequency. The plot shows the detection counts measured on a PMT. 20 Measurements where made for wait times (t) between 7 and 9 ms. Red shows a microwave Ramsey with no 355 nm light on the ions. Blue shows the same Ramsey experiment with 355 nm light aligned to the ions. Error bars (for both red and blue) represent the standard deviation of the bright state detection florescence for the 20 data points in each experiment. Fit function: $A\sin^2\left(\frac{\pi t}{2T}\right)$ + offset where $\pi-$time $= T$. 31

3.11 **Resonant microwave Ramsey with** 355 nm **light.** Data points (blue) are the average detection counts measured on a PMT (100 experimental repetitions) while performing a resonant microwave Ramsey experiment with the 355 nm laser shining on the ions through RP2. Error bars represent the standard deviation of the bright state detection florescence for the 20 data points in the experiment. These oscillations are due to the AC Stark shift from the 355 nm light and are measured to be on the order of $\omega/2\pi =$ 300 Hz while sending approximately 150 mW of optical power. Fit function: $A\cos^2(\omega t)$ + offset. 32

3.12 **Cylindrical lens alignment.** The left shows the 355 nm beam centered on the ions. In this configuration, moving the ions left and right of center would show a symmetrical decrease in Rabi frequency, regardless of the alignment of the horizontal beam waist to the ion chain. The right shows the 355 nm beam displaced from the center ion. In this case, moving the ions left and right of center would show a symmetrical Rabi frequency only in the case where the horizontal beam waist is aligned to the ion chain. Ions not to scale. 33

3.13 **Raman carrier flopping.** Y-axis displays the probability of finding the qubit in the $|\uparrow\rangle$ state (normalized by performing a microwave π rotation to account for fluctuations in the detection laser's intensity). X-axis shows the amount of time that the 355 nm lasers were applied to the ion while addressing the carrier transition. Error bars show the standard error over 100 experimental repetitions. Fit function: $\cos^2(\omega x)\left(Ae^{-x/\tau} + B(1-e^{-x/\tau})\right)$ where $\pi-$time $= \pi/(2\omega)$. 34

3.14 **Ion fluorescence while applying a MS scheme.** Y-axis displays PMT counts for a detection time of 400 μs while the x-axis shows the amount of time the MS laser scheme was applied to the ions. Error bars show the standard error over 100 experimental repetitions.
Fit function: $\sin^2(\omega x)\left(Ae^{-x/\tau} + B(1 - e^{-x/\tau})\right)$ where $\pi-\text{time} = \pi/(2\omega)$. . 35

4.1 $^{171}Yb^+$ **detection transition**. A 369.5 nm laser is turned to the cycling transition of the $F = 1$ to $F' = 0$ state. With some probability, the photons emitted when the atom decays will be detected by a PMT or camera. Δ_{HFS} and Δ_{HFP} are the hyper-fine splittings of the S and P manifold, respectively. 42

4.2 **Blade trap imaging layout.** Ion fluorescence is shown in purple while ion addressing from the DMD, 355 nm, and ionization beams are shown in blue. Two 0.5 NA custom made objectives from Photon Gear (P/N:18910) make up the symmetric two-sided imaging of the blade trap. A parabolic reflector will be mounted on a flip mirror to help align the 1 μm Raman beam to the ions. A flip mirror with a concave surface will be used to direct light on the a PMT detector for fast individual mid-circuit measurement. The top imaging system uses a 0.3 NA objective from Special Optics (P/N 1-293434) and will be used for experiments that require both mid-circuit measurement and global camera detection. The same objective will be used on the bottom to provide an unchanging reference to the ion while also making the alignment of the DMD to the ion easier. 45

4.3 **State detection fidelity vs detection beam intensity.** Above is a plot of state detection fidelity vs detection beam intensity (I/I_{sat}) for different detection times. The grey region represents our target state detection fidelity of 99.9%. Calculations include system efficiencies and a background scattering rate of 50Hz, the limit coming from the PMT's dark count as quoted from the data sheet. 51

4.4 **Background scattering rate.** The above colour map shows state detection fidelity vs background scattering rate and detection light intensity. Simulations include the effects from system efficiencies with a detection time of 25 μs. The dashed line indicates the typical dark count for the PMT (50 Hz). 52

4.5 **Effect of lenses on state detection fidelity.** The above colour map shows state detection fidelity vs number of Fused Silica lenses and detection light intensity. Simulations include the effects from system efficiencies with a detection time of 25μs. The dashed line indicates the number of lenses in our current mid-circuit measurement system (2). 53

4.6 **CAD design for the blade trap imaging system.** The left shows the full assembly with vacuum chamber and 3$^{\text{rd}}$ floor blase plates used to mount the DMD and top imaging systems. The right shows a close up of the side objective mounting. 55

4.7 **Doublet simulations.** The above shows the Zemax simulation for the doublet in the blade trap imaging system that focuses the beam down to IP1. a) is a optical schematic showing the custom made 0.5 NA objective from Photon Gear (represented as a black box optics files) and doublet. b) shows the fractional enclosed energy as a function of radial distance. c) shows the spot diagram at IP1 for fields from center to 200 μm in steps of 50 μm. The Seidel diagram (d) shows the optical aberrations introduced at each lens surface and summed at IP1. 59

4.8 **Doublet simulations.** The above shows the Zemax simulation for the full blade trap imaging system to the qCMOS camera. a) is a optical schematic showing the doublet and relay imaging system. b) shows the fractional enclosed energy as a function of radial distance. The dashed line indicates the size of a single pixel on our camera's detector (4.6 μm $\times$ 4.6 μm). c) shows the spot diagram at the camera sensor for fields from center to 200 μm in steps of 50 μm. The Seidel diagram (d) shows the optical aberrations introduced at each lens surface of the relay system. 61

4.9 **Doublet test setup.** The above shows the setup used to test the performance of the doublet. An SNOM fiber with a 100 nm aperture was used to mimic the ion acting as a point source. The 0.5 NA objective was placed inside the re-entrant and aligned to the fiber. An FLIR camera with a square pixel size of 1.85 μm was used to image the fiber at IP1 after the doublet. . 62

4.10 **Doublet testing measurements.** a) shows the initial beam focused after the doublet focused onto a FLIR camera while b) shows the final result after alignment was complete. c) shows the measured and simulated values for the enclosed energy. Multiple measurements where taken for different beam intensities and slight shifts in objective-fiber focus and were used to get the min-max error bars. The simulated data for the enclosed energy was taken from the Zemax simulations for the doublet. 63

5.1 **Current status of the new lab in B221A.** The 2.5 ft and 5 ft optics tables for the lasers and blade trap system respectively have been place into position. The optics table enclosure frame is mostly installed and is halted until the construction of the air vents is complete. 68

List of Abbreviations

AMO Atomic Molecular and Optical 3, 16

AOD Acousto-Optic Deflector 50

AOM Acousto-Optic Modulator xi, 18, 19, 25, 26, 33, 50

AR Anti-Reflective 49, 54

AWG Arbitrary Waveform Generator 15

BSB Blue Side-Band ix, 12, 13

CAD Computer Aided Design 14

cps counts per second 53

CW Continuous-Wave 13

DC Direct Current iii, viii, x, xi, 4, 14, 19–23, 28, 38, 67

DMD Digital Micro-mirror Device xiii, xiv, 15, 16, 40, 45, 47, 48, 55

E-S-C Environmental Systems Corporation 17

ECDL External-cavity Diode Lasers viii, 2

EOM Electro-Optic Modulator 18

FS Fused Silica 25, 46, 49, 54

HVAC Heating, Ventilation and Air Conditioning ix, 17

MS Mølmer–Sørensen ix, xiii, 3, 12, 35, 36, 67

NA Numerical Aperture viii, xiii, xiv, 4, 5, 39, 40, 45–48, 59, 62–65

NISQ Noisy Intermediate-Scale Quantum 1

PBS Polarizing Beamsplitter 25

PETG Polyethylene Terephthalate Glycol 28

PLA Polylactic Acid 28

PMT Photonmultiplier Tube xii, xiii, 5, 31, 32, 35, 39, 41, 42, 45–47, 49–54, 56, 66, 68

QNC Quantum-Nano Center 15

RF Radio Frequency viii, 1, 3, 4, 7, 19, 36, 38, 50, 67

RP1 Raman path 1 xi, 25, 26, 30, 32–34

RP2 Raman path 2 xi, xii, 25, 26, 29, 30, 32, 34, 38

RSB Red Side-Band ix, 12, 13

SHO Simple Harmonic Oscillator 7

SMA SubMiniature version A ix, 18, 19

SMPS Switch Mode Power Supplies 21, 23

SNOM Scanning Near-field Optical Microscopy xiv, 62, 63

SNSPD Superconducting Nanowire Single-Photon Detector 41, 53

UHV Ultra High Vacuum 3, 5

w.r.t. with respect to ix, 18

XHV Extreme High Vacuum 5, 15, 36, 68

Chapter 1

Introduction

As our understanding of the universe grows, we require increasingly powerful tools to simulate its behaviour. In the current era of Noisy Intermediate-Scale Quantum (NISQ) computers, quantum simulators have emerged as a promising avenue for exploring the behavior of some quantum systems that are otherwise inaccessible or uncontrollable [2]. For a system to meet the minimum requirements of a quantum simulator we must be able to prepare the initial conditions, evolve the system in a repeatable fashion, and measure the states of the system. While these are the minimum requirements a quantum simulator must meet, there are a number of tools that can expand the capabilities of the system. The ability to perform measurements of specific qubits without destroying the state of the neighbouring qubits during a quantum simulation (referred to as mid-circuit measurement) is one such tool that opens the doors to new areas in physics such as measurement induced phase transitions. These phase transitions study area to volume law transitions in the entanglement entropy by introducing projective measurements on a subset of evolving qubits [3].

As a quantum simulator, the trapped ions platform make an excellent candidate. Long coherence times, all-to-all connectivity, and high fidelity state preparation and measurement, are some of the characteristics that set trapped ions apart from other platforms. With recent results demonstrating a high degree of control [4] and high fidelity individual qubit addressing [5], the trapped ions platform provides the ideal candidate for simulating these measurement induced phase transitions [6]. To build a system capable of performing such experiments will come with an increase in complexity. Trapped ions rely on vacuum chambers, lasers, Radio Frequency (RF) electronics, and many more systems working in unison to perform even the most basic of quantum simulations. Figure 1.1 shows many of the systems required to perform these basic quantum simulations. These systems must be

designed and engineered to be robust if we are to realize the full potential of the trapped ions platform as a quantum simulator.

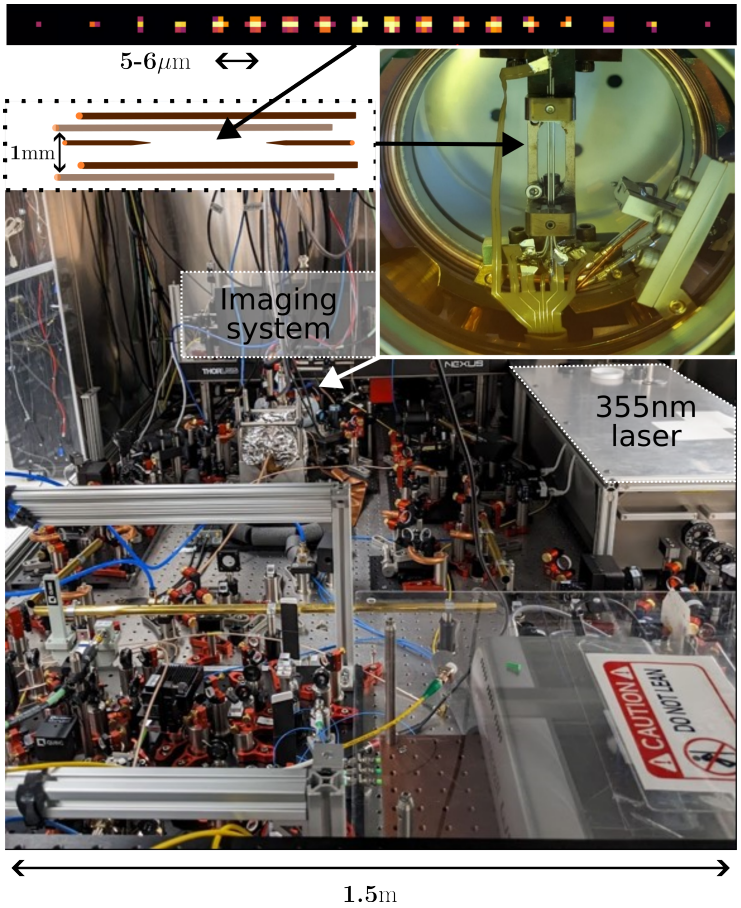


Figure 1.1: **Four-rod trap quantum simulator.** Near the center of a 5ft $\times$ 10ft optics tables sits a four-rod Paul trap (upper right) inside a vacuum chamber. Along the top shows a linear chain of 18 $^{171}Yb^{+}$ ions trapped in this apparatus. ECDL (not visible in the image) generate laser light which is prepared (bottom left) and delivered onto the ions to perform various operations like Doppler cooling and state detection. Light from a 355 nm pulsed laser (middle right) is split into two paths and brought to the ions to perform coherent operations. An imaging system (center back) collects photons emitted from the ions for state detection.

1.1 Four-rod trap quantum simulator

Our first quantum simulator comes in the form of a four-rod Paul trap [7] contained in a Ultra High Vacuum (UHV) chamber with a pressure of about 2×10^{-11} mbar. The trap, shown in the upper right corner of Figure 1.1, follows closely the design in [8], with improvements to the fabrication of the end needles [9], and was built by the lab member of the time.[1] The four-rod trap was optimized to trap an isotope of Ytterbium, $^{171}Yb^{+}$ and serves as a platform to test various systems including an aberration corrected addressing system [10].

The pillar of any experiment, quantum or otherwise, is the infrastructure of the lab. Ion traps, as well as other Atomic Molecular and Optical (AMO) labs, require vacuum systems, RF electronics, lasers and optics (seen in Figure 1.1) which put high demand on the lab infrastructure. Providing stable temperature and humidity conditions in a lab is required for stabilizing a laser's frequency, maintaining polarization in a fiber and reducing drifts in laser beam pointing. Clean voltages to supply current to equipment and proper grounding is required to reduce noise that can disrupt sensitive experiments. Part of this thesis aims to address the critical need for designing and implementing the robust lab infrastructure required for trapped ion quantum simulators. By engineering enclosures and incorporating water cooling of equipment, plans are made to provide an environment capable of stabilizing to $\pm 0.1°$C and roughly $\pm 1\%$ relative humidity.

Generating controllable entangling operations is an essential tool for many trapped ions quantum simulators. These operations are typically done by exciting stimulated Raman transitions which couple the qubit spin to the motional mode of the ion chain to drive XX-type spin interactions.[2] Engineered optical controls give the precision needed to align the four-rod trap Raman laser beam to the ion in order to drive entangling operations. By setting our lasers to drive a Mølmer–Sørensen (MS) operation [11] we are able to achieve $5-6$ flops from $|\downarrow\downarrow\rangle$ to $|\uparrow\uparrow\rangle$ before the system decays.[3] By overcoming challenges posed by environmental noise and instability, experimental imperfections, and technical constraints, a system capable of performing complex quantum simulations such as dissipative spin cooling [12] is built. The development of these robust systems used in the four-rod quantum simulator will be covered in Chapter 3.

[1] Those lab members include: Nikhil Kotibhaskar, Sainath Motlakunta, Chung-You Shih, Manas Sajjan and Roland Habluetzel.

[2] XX-type interaction are of the form $H = \sum_{i,j} J_{ij} \sigma_x^i \sigma_x^j$ where J_{ij} denotes the strength of the interaction between ions i and j.

[3] Before the amplitude of the flops decays by a factor of $1/e$.

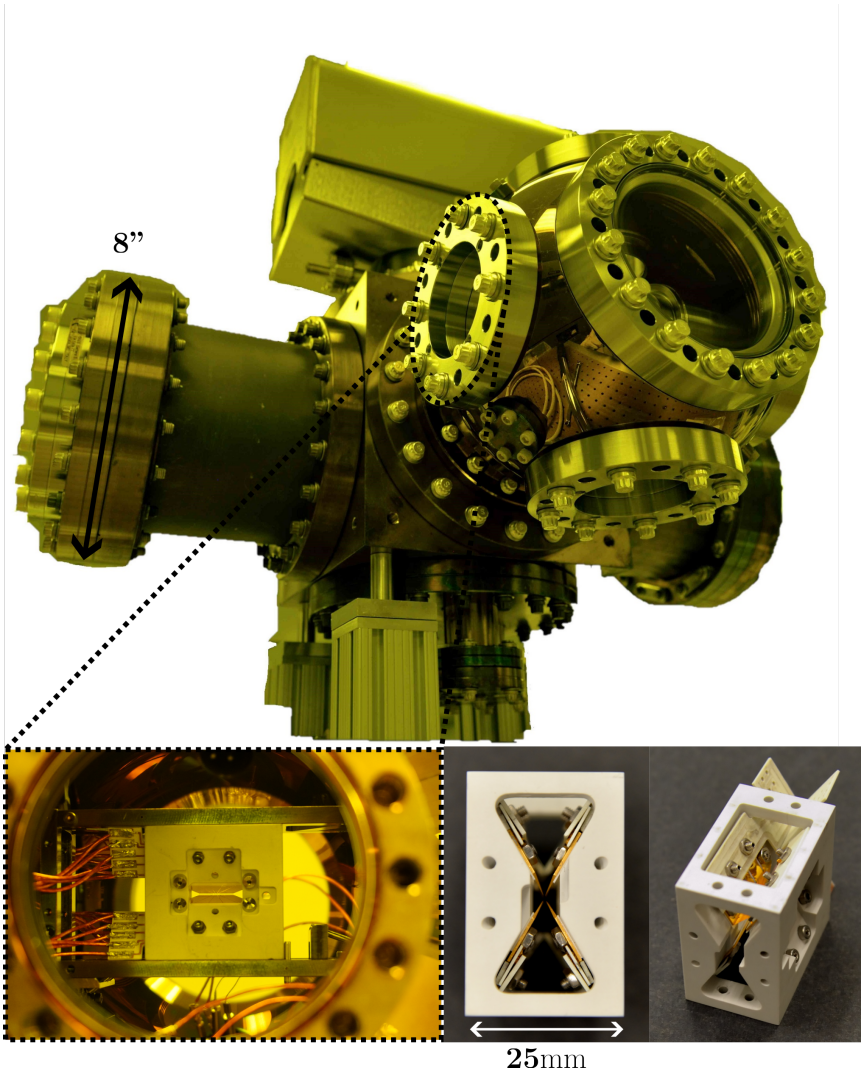


Figure 1.2: **Blade trap vacuum assembly and internals.** The top image shows the vacuum assembly for the blade trap. A front facing window and four re-entrant windows provide optical access to address and image the ion. Bottom left shows a side view of the segmented blade trap. Wires carry RF and DC voltages to confine and control the ion. The bottom center shows the front facing view of the blade trap. The gold coated segmented blades are positioned to give 0.5 NA optical access from the sides and 0.3 NA from the top and bottom and are held in place with the Shapal blade holder.

1.2 Blade trap

While the four-rod trap has proven to be a great test bed for ideas such as an aberration corrected addressing system [10], limitations in optical access and increased background pressure make quantum simulations of six or more qubits challenging if not impossible. In parallel to the four-rod experiment our team has been developing a meticulously engineered trapped ion quantum simulator in the form of a blade trap. By using four, segmented blades (seen in the lower left of Figure 1.2), in place of four rods and two needles, we achieve more control over the ions in the trap.[4] The vacuum chamber and internal assembly (including the segmented blade trap) can be seen in Figure 1.2. With much higher photon collection efficiency and more robust optics, we plan to be able to perform quantum simulations on more than 30 qubits. With an increase in the number of qubits, we become more susceptible to background collision events from the atoms left in the chamber, which can be violent enough to kick ions from the trap. To sustain an average ion lifetime on the order of an hour we must reach vacuum pressures on the border of UHV and Extreme High Vacuum (XHV).[5] To reach such low pressures, the vacuum chamber and each component inside needs to be diligently prepared to reduce the out-gassing rate that leads to higher background pressures. In the end of Chapter 3 this thesis will cover the preparation of the ceramic blade holder that was completed to sustain a base pressure of 9×10^{-13} mbar.

Implementing an imaging and addressing system that enables in-situ[6] mid-circuit measurement would significantly enhance the capabilities of the blade trap system. As mentioned earlier, this would open the doors to exploring new physics such as measurement induced phase transitions. To perform mid-circuit measurement on systems of roughly 30 qubits we require a high state detection fidelity with low detection times to avoid cross-talk between neighbouring ions in the simulation. Another advantage to using blades in place of rods for the trap is the increase in optical access to the ions, an essential ingredient for high fidelity state detection. In this thesis I will design a high NA imaging system with emphasis on achieving high state detection fidelity with a Photonmultiplier Tube (PMT) detector. I simulate the system and determine that detection times on the order of 20 to 40 μs should be possible with optimal conditions in the dual imaging of the blade trap system. As we will see, these detection times are required when performing mid-circuit measurement in a system such as the blade trap. Throughout my testing, I find that background scattering from the ion address beam will be the dominating contribution to

[4] A detailed description of the blade trap design can be found in Sainath Motlakunta's PhD thesis [1].

[5] Here we are taking the convention that UHV pressures are between 10^{-8} to 10^{-12} mbar while XHV pressure is anything below 10^{-12} mbar.

[6] in place

lower detection fidelity. Chapter 4 will cover my work developing the blade trap imaging system.

1.3 Outline

The following will outline the contents of this thesis:

- **Chapter 2:**
  This chapter will briefly cover the physics of trapped ions to provide a foundation for the following chapters. It will start by covering the processes of trapping and state initialization of the $^{171}Yb^{+}$ ion. It then looks at coherent controls, including single qubit rotations as well as entangling operations. Discussions on state detection will be held until Chapter 4.

- **Chapter 3:**
  In this chapter, we will explore the details of building robust systems that are needed in a trapped ion quantum simulator. We will start with a brief history of the lab so as to avoid confusion in the later sections. We will then turn to the infrastructure of the lab and move onto the controls that are necessary to drive entangling operations in our qubits. Lastly, we will examine the work that has been done on the next generation of ion traps, and will explore ways of increasing ion lifetimes by reducing background collision rates.

- **Chapter 4:**
  In Chapter 4 we will start by revisiting the physics of detecting an ion and the influences of various parameters on state detection fidelity. We will then look at the proposed layout for the blade trap imaging system, and explore the requirements for the system. We will look at the mechanical and optical engineering required to build a robust imaging system before performing the initial test of said system.

- **Chapter 5:**
  Chapter 5 will conclude the thesis and provide the current status of the blade trap and new lab space.

Chapter 2

Trapped ion physics

As is tradition in any graduate thesis on trapped ions, this chapter will outline some of the physics of trapped ions. It will focus specifically on $^{171}Yb^{+}$ and the geometry of our current 4-rod trap.

2.1 Trapping and state preparation

Like many ion traps before it, our system relies on an oscillating electric field to create a confining pseudo-potential in the radial direction. This is commonly referred to as a Paul trap, named after it's inventor, Wolfgang Paul [7]. As the name suggests, our four-rod trap creates this pseudo-potential by applying RF voltages on tungsten rods which are suspended inside a vacuum chamber. Constant voltage is applied to needle electrodes in order to achieve proper confinement in the axial direction. The effect of these electric fields on the ion scale can be modeled after a Simple Harmonic Oscillator (SHO) giving rise to the effective potential:

$$\phi_{eff} = \frac{1}{2} m \left(\omega_x^2 x^2 + \omega_y^2 y^2 + \omega_z^2 z^2 \right) \tag{2.1}$$

where m is the mass of the particle (ion). To create a one dimensional, linear chain of ions, we ensure that the radial frequencies (ω_x and ω_y) are much greater than the axial frequency (ω_z), namely $\omega_x \approx \omega_y \gg \omega_z$.[1] For our 4-rod trap $\omega_x, \omega_y \approx 2\pi \times 1$ MHz and $\omega_z \approx 2\pi \times 100$ kHz.

[1] To break the degeneracy between the two radial trap frequencies we apply a bias voltage to the rods of one axis so that $|\omega_x - \omega_y| \approx 2\pi \times 100$ kHz.

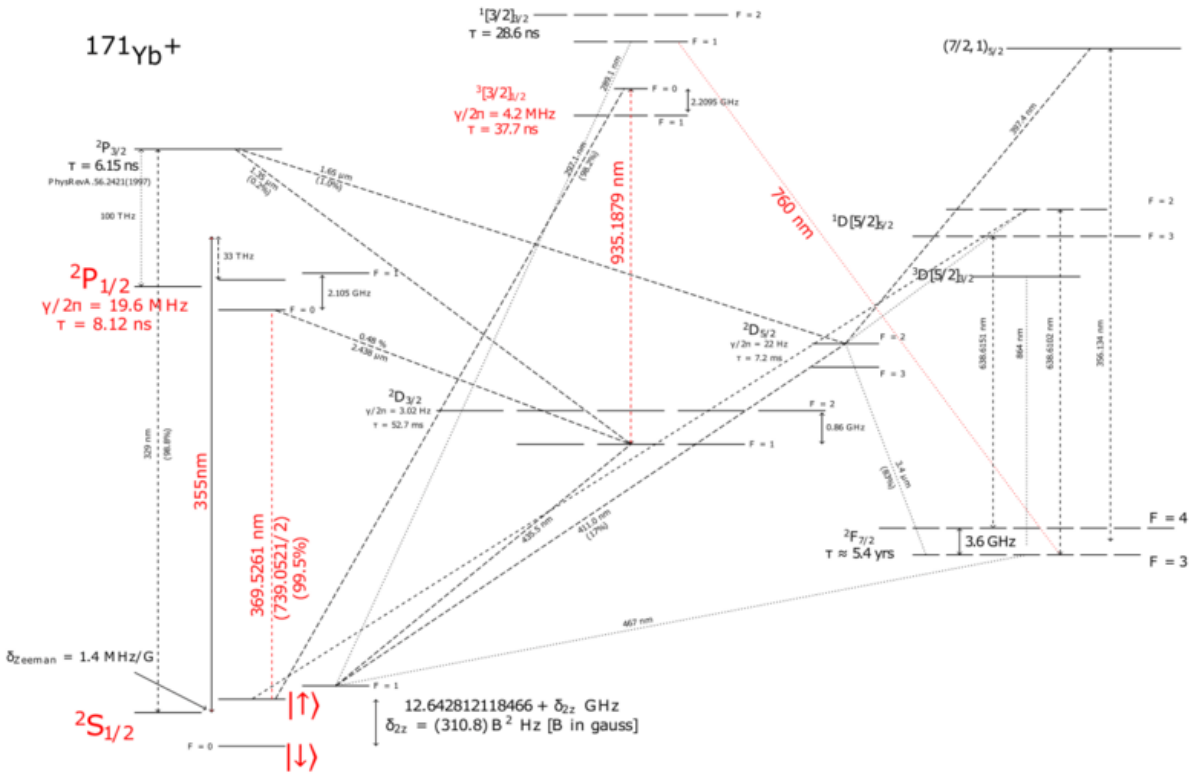


Figure 2.1: **Internal energy level diagram of** $^{171}Yb^{+}$ [1]. The red text shows the primary transitions used in the 4-rod trap system.

To generate ions, we start by applying current to one end of a small hollow, stainless steel tube filled with Ytterbium, which locally heat the sample. This localized heat creates an oven that shoots neutral atoms towards the trap's center. A 399 nm laser is used to excite an isotope-dependent internal electronic energy state of the neutral Ytterbium (this is referred to as first ionization). Then, either 369 nm or 355 nm light is used to kick the electron from the excited state in the atom, producing a positive ion of the desired isotope. By overlapping these beams with the center of the four rods and two needles, we are able to trap various isotopes of Ytterbium. One isotope in particular, $^{171}Yb^{+}$, gives an energy structure that is suitable for quantum simulations. This energy structure can be seen in Figure 2.1. To treat our ion as a two-level system, we must remove energy thereby cooling our ion. We can do this by applying a laser beam that is focused on the ion, with

a frequency that is detuned from an internal energy transition by an amount δ (30 MHz in the case of our four-rod trap). Due to the ion's motion in the trap, it will see the frequency of the laser Doppler shifted and on resonant with the transition only when its motion is against the direction of the laser beam.[2] When the ion absorbs these on resonant photons, it gets a small kick in momentum, thus slowing it down. If this is a relatively short lived state (10's of ns), the ion will decay back to the ground state by means of spontaneous emission. This emission of a photon occurs in random direction, so after many iterations, it will average to zero momentum transfer. Figure 2.2 shows the commonly used cooling transition in $^{171}Yb^{+}$ using a 369 nm laser to drive the ion from the $^2S_{1/2}$ to $^2P_{1/2}$ manifold, the lifetime for which is approximately 8 ns.

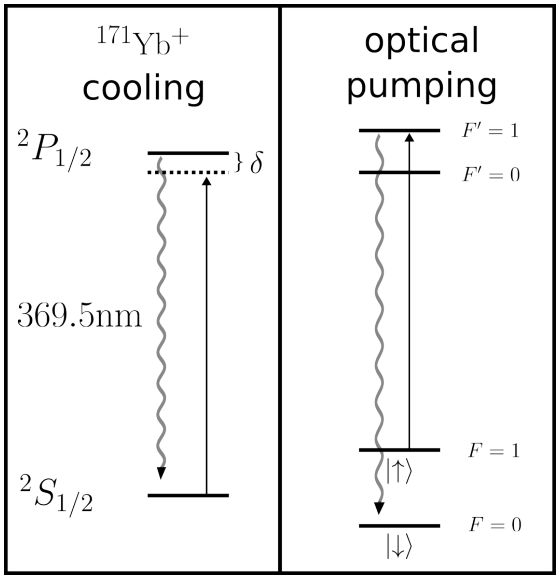


Figure 2.2: $^{171}Yb^{+}$ **cooling and state initialization transitions.** The left shows the $^2S_{1/2}$ to $^2P_{1/2}$ transition used for Doppler cooling. The hyper-fine and Zeeman levels are not shown here for simplicity. The 369.5 nm laser is detuned from the $^2P_{1/2}$ states by $\delta = 30$ MHz in our four-rod trap. The right diagram includes the hyper-fine levels of the S and P manifold used for state initialization (optical pumping). A 369.5nm laser is tuned to the $|\uparrow\rangle$ ($|F = 1\rangle$ state) to $|F' = 1\rangle$ transition. Once in the excited state, the ion has an approximate 1/3 probability of decaying to the $|\downarrow\rangle$ ($|F = 0\rangle$) state.

With the ion now cooled, we choose the two hyper fine states $^2S_{1/2}\,|F = 0, m_F = 0\rangle$ and $^2S_{1/2}\,|F = 1, m_F = 0\rangle$ to form our effective spin $\frac{1}{2}$ system labeling them $|\downarrow\rangle$ and $|\uparrow\rangle$

[2] If we've properly detuned our laser.

respectively. The transition used for state initialization (often referred to as optical pumping) can be seen in Figure 2.2. To prepare our system in the $|\downarrow\rangle$ state, we again apply our 369 nm laser to the ions; this time, tuned to the frequency difference between the $^2\mathrm{S}_{1/2}\,|F=1, m_F=0\rangle$ and $^2\mathrm{P}_{1/2}\,|F'=1, m_F=0\rangle$ levels. Once in the excited state, the ion has a 1/3 probability of decaying to the $|\downarrow\rangle$ state. We leave the detailed discussion of detection until Chapter 4. For now, we will simply state that there exists a cycling transition that allows us to determine the state of our ion by collecting the fluorescence from emitted photons.

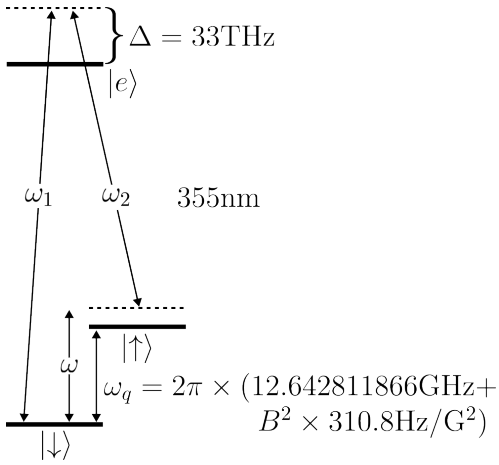


Figure 2.3: **Energy level diagram for driving stimulated Raman transitions.** Two laser frequencies from a 355 nm pulsed laser, ω_1 and ω_2 are detuned from the excited state, $|e\rangle$ by an amount $\Delta = 33\mathrm{THz}$. Here $\omega = |\omega_1 - \omega_2|$ is the frequency difference between the two lasers, while $|e\rangle$ is the $^2\mathrm{P}_{1/2}$ manifold in our four-rod trap.

2.2 Single qubit rotation

There are two methods of performing coherent rotations of our qubit. The first uses microwave magnetic fields which couple to the magnetic dipole moment. If the frequency is tuned near the qubit frequency, $\omega_q \approx 2\pi \times 12.6$ GHz, we will drive Rabi oscillations from the $|\downarrow\rangle$ state to the $|\uparrow\rangle$ state. Flopping using microwave in this way provides high fidelity preparation of the ions in the $|\uparrow\rangle$ state, but has some limitations. Due to the long wavelengths ($\approx$ 2 cm) microwave fields cannot be focused down tightly enough to individually address ions, making it a global operation. As we will see in the next section,

the primary scheme used to entangle qubits is mediated by exciting phonon modes. The momentum in the microwave field is insufficient for exciting these modes, thus making it a single qubit operation only.[3]

The other way to drive qubit rotations is by stimulated Raman transitions. These use two optical frequencies ω_1 and ω_2 (~ 355 nm) to couple the spin states to an excited state $|e\rangle$ which for $^{171}\mathrm{Yb}^+$ is the $^2\mathrm{P}_{1/2}$ manifold. The laser frequencies are far detuned ($\Delta \approx 33$ THz for $^{171}\mathrm{Yb}^+$) from the the excited state to minimize the population transfer to it.[4] To couple to this excited state, we require either σ^+ or σ^- polarized light [14]. This leads to the requirement that our two laser beams have polarization that is linear, perpendicular to the ions quantization axis, and perpendicular to each other. This scheme is often referred to as 'lin-perp-lin'. For simplicity, we define the difference of our two lasers' frequencies as $\omega \equiv \omega_1 - \omega_2$. By setting the laser frequencies such that $\omega = \omega_q$ and addressing the ion with this light, we create the following Hamiltonian:[5]

$$H_{carrrier} = \frac{\Omega}{2}\left(\sigma^+ e^{i\phi} + \sigma^- e^{-i\phi}\right) \tag{2.2}$$

Here, $\Omega = \frac{\Omega_1\Omega_2}{\Delta}$ is the effective Rabi frequency with Ω_1 and Ω_2 being the Rabi frequencies from the two laser frequencies. σ^+ (σ^-) is the spin raising (lowering) operator and ϕ is the phase difference between the two laser beams. When applied to the ion in our configuration, we drive Rabi oscillations between our two spin states. This process is often referred to as carrier flopping. If, instead, we set $\omega = \omega_q - \omega_x$ [6] our Hamiltonian becomes:

$$H_{RSB} = \frac{\Omega\eta}{2}\left(\sigma^+ a e^{i(\phi+\frac{\pi}{2})} + \sigma^- a^\dagger e^{-i(\phi+\frac{\pi}{2})}\right) \tag{2.3}$$

The subscript RSB is short for red side band and comes from being lower in frequency, and thus 'red' detuned from the carrier transition. The Lamb-Dicke parameter η is a quantity used in the trapped ion community to compare the spread of the ion's spatial wave function to the wavelength of the laser's light, and is typically much less than one for our applications [16].[7] $a^\dagger$ (a) is the creation (annihilation) operator which acts on our

[3] There are schemes that have gotten around both of these limitations. However, they require complex traps and/or setups to do so. [13]

[4] There are also contributions from the $^2\mathrm{P}_{3/2}$ state for which the lasers are ≈ 66 THz detuned from.

[5] For a complete derivation starting from the effects of an Electric field on a dipole (ion) and the regimes for which it holds see [15] or [16]

[6] Recall ω_x is one of our radial trap frequencies. We could also have set $\omega = \omega_q - \omega_y$.

[7] $\eta = \Delta k\sqrt{\frac{\hbar}{2m\omega}}$ where Δk is the difference in our two laser's wave vector.

ions motional-mode ie. $a^\dagger |n\rangle = \sqrt{n+1}\,|n+1\rangle$ ($a\,|n\rangle = \sqrt{n}\,|n-1\rangle$). Lastly, if we set $\omega = \omega_q + \omega_x$ we get our Blue Side-Band (BSB) Hamiltonian as:

$$H_{BSB} = \frac{\Omega\eta}{2}\left(\sigma^+ a^\dagger e^{i(\phi+\frac{\pi}{2})} + \sigma^- a e^{-i(\phi+\frac{\pi}{2})}\right) \tag{2.4}$$

These last two Hamiltonians have the effect of flipping an ion's spin state, while also increasing or decreasing its motional-mode. This forms spin-motion coupling which we can use to entangle ions together as we will briefly touch on in the next section.

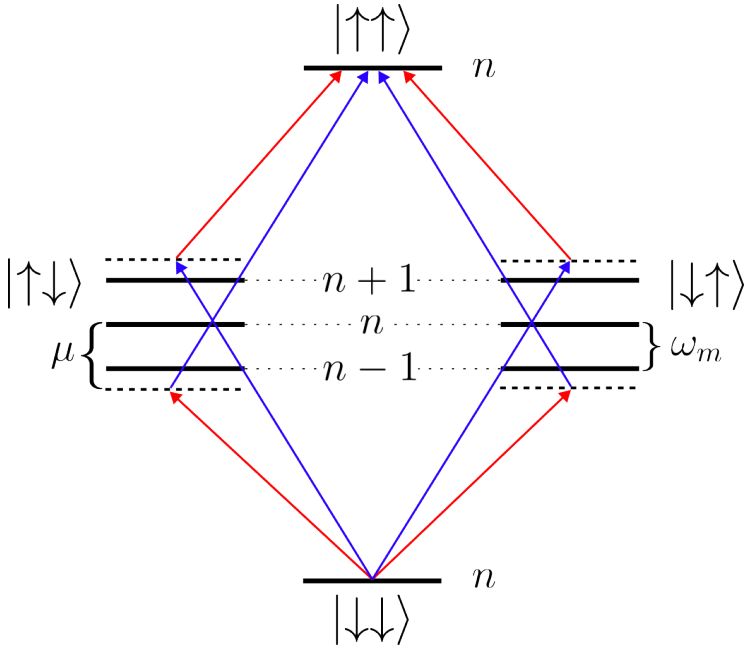


Figure 2.4: **Mølmer-Sørensen level diagram.** Here, ω_m is the frequency of the m$^{\text{th}}$ motional mode and μ is the lasers detuning, referred to as the MS detuning. Red and blue arrows indicate the symmetrical detunings of the RSB and BSB Raman transitions needed to drive flopping from $|\downarrow\downarrow\rangle$ to $|\uparrow\uparrow\rangle$.

2.3 Entangling operations

A robust way to generate entanglement in trapped ion systems was first proposed by Klaus Mølmer and Anders Sørensen [11]. As suggested in the last section, the MS scheme

relies on spin-motion coupling that is generated from the stimulated Raman transitions. Figure 2.4 shows the level diagram and lasers required to drive the entangling operation. By addressing the ions with both the RSB and BSB transitions, slightly detuned from a motional-mode of the ion chain, we are able to drive flopping from $|\downarrow\downarrow\rangle$ to $|\uparrow\uparrow\rangle$. The result of this MS scheme (in the correct regime) creates the effective Hamiltonian:

$$H_{MS} = \sum_{i,j} J_{ij} \sigma_i^x \sigma_j^x \tag{2.5}$$

For our purposes in this thesis, we will simply note that $J_{ij} \propto \Omega_i \Omega_j$, the Rabi frequencies of ions i and j respectively. For a detailed derivation of the MS scheme and the regimes for which it holds, see ref. [15] or ref. [16].

2.4 Implementing Raman transitions

Before moving on, we will briefly discuss how we drive our Raman transitions in the 4-rod system. As mentioned above, we require two wavelengths around 355 nm that are separated in frequency by roughly the qubit frequency (12.6 GHz). One option would be to have two separate Continuous-Wave (CW) lasers that can be tuned to achieve this frequency difference. This is difficult in practice, since both lasers must be phase-coherent while also supplying the high intensity light required to drive these transitions. We chose, instead, to adopt the more common practice of using a pulsed laser with a repetition rate of 80.34 MHz. This repetition rate has been carefully chosen so that the zeroth (fundamental) and 157^{th} peak are approximately 12.6 GHz. By splitting the 355 nm light into two separate paths, we can precisely tune the frequency to achieve the transitions from above. As the pulses have a spread of only a few millimeters, we have to precisely tune the lengths of each path to match (within 10's of microns for strong Raman transitions). Since the repetition rate of the laser is not perfectly stable, we have a feed-forward system installed in one of the paths to correct for the variations in the pulse width. [17].

Chapter 3

Designing robust systems

Now that we have an understanding of the physics of trapped ions, we can design a system capable of performing a wide range of quantum simulations. In this chapter, I will discuss the various systems I have worked on that aim to make our experimental system more robust.

- **Section 3.1:** I will give a brief history of the lab which will be used to motivate the work in the following sections.
- **Section 3.2.1:** Will cover my work designing in Computer Aided Design (CAD) software the optics table enclosures, and constructing the water cooled amplifier box. I'd like to thank Gaurav Ashish Tathed for his help in assembling the water cooled amplifier box.
- **Section 3.2.2:** Will cover cover the work I've done designing, installing and testing the DC power distribution and grounding systems in B221B. Implementing these systems into our lab provides our four-rod trap quantum simulator with clean DC voltages while minimizing the possibility of grounds loops that can introduce noise. I'd like to thank Nikhil Kotibhaskar for his contributions to the design of the power distribution system. I'd also like to thank Rich Rademacher for his work designing the DC power distribution boards that are used in the system.
- **Section 3.3:** Will cover my work building, aligning and testing the laser and optical systems used to drive Raman transitions in our four-rod trap. Controls developed in Section 3.3.2 and techniques implemented in Section 3.3.3 lead to the ability to drive two-qubit entangling operations shown in Section 3.3.4. I'd like to thanks Jingwen

Zhu (Monica) for her work aligning the first path of the four-rod trap Raman system. I'd like to thank Sainath Motlakunta for his work designing the lens system for the Raman system. I'd also like to thank Chung-You Shih for his work integrating the Arbitrary Waveform Generator (AWG) into the control system which was required to preform the entangling operations.

- **Section 3.4:** Will cover the work I've done to improve our blade traps vacuum pressures by reducing the out-gassing rate of the Shapal blade holder. With the out-gassing of the blade holder reduced, we where able to reach our requirements of XHV needed to increase ion life-times. The work in this section would not be possible without the extensive work done by Nikhil Kotibhaskar to design, simulate and prepare a vacuum chamber capable of these pressures.[1] I'd also like to thank Sainath Motlakunta for his critical role in assembling the blade trap vacuum system, and for his help in monitoring the baking of the blade holder.

3.1 History

Our current system, a four-rod Paul trap with two needles, sits on a 5ft by 10ft Newport optics table in B221B, a basement room located in the Quantum-Nano Center (QNC) at the University of Waterloo. The trap offers a platform for us to develop and innovate new systems that can then be built into a more capable ion trap. One such system, is our aberration corrected individual qubit addressing system. Using a Digital Micro-mirror Device (DMD) we create a diffraction pattern in the Fourier plane of the addressing system. By taking the first order beam at an intermediate image plane, we are able to get full phase, position, and amplitude control of the light on our ion [10]. We then use the $^{171}Yb^{+}$ ion as a near perfect point source sensor to create a phase map of our system. We can then correct for these aberrations by setting the appropriate DMD profile to get a diffraction limited beam on our ion. With this system, we have been able to show that high fidelity in-situ individual measurement and state reset is possible on the trapped ions platform [12].

As the capabilities of our 4-rod trap have increased, we have pushed the system to perform more complicated and precise experiments. These experiments have revealed inherent instabilities within the system and limit our experiments with the four-rod trap to six or fewer qubits. An example of this is seen within the system responsible for temperature

[1] An in-depth look into designing a room temperature ion trap capable of reaching these pressures will be detailed in Nikhil Kotibhaskar PhD thesis.

and humidity stabilization in the lab, which works by exchanging the heat with the building chilled water. Due to the system being undersized, the lab can see temperature fluctuations of $\pm 0.5°\mathcal{C}$ and humidity variations of $\pm 10\%$ in the span of an hour. These fluctuations lead to instabilities in beam alignment, laser mode, and frequency measurements, all of which limit the scientific gains we are able to achieve.

In parallel to the 4-rod trap, we have been developing and engineering a blade trap system, with hopes of performing quantum simulations on more than 30 qubits. The blade trap is currently in the final stages of internal vacuum assembly. In order to expand our quantum simulation capabilities, the blade trap will be equipped with larger trap frequencies, higher NA imaging, and individually addressable two-qubit operations, along with the DMD addressing from the 4-rod system. With this system, we now have the opportunity to build a new lab space in an adjacent room, B221A,[2] from the ground up, by taking what we have learned from our 4-rod system and improving on it.

3.2 Lab infrastructure

While it may not be the most exciting part of an experiment, lab infrastructure serves as the pillar for which any experiment can be conducted, whether it be quantum or otherwise. Depending on the sensitivity and complexity of an experiment, the requirements for a lab's infrastructure can vary from a level floor all the way to the cleanest of clean room environments. An ion trap, and many other AMO physics labs, require vacuum systems, electronics, radio frequency and microwave generators, lasers that span the infra-red to ultra-violet range, as well as the optics to shape the light. These requirements mean that AMO physics labs can be some of the most complex and demanding, requiring robust lab infrastructure to unlock their full potential in running quantum simulations. With an opportunity to start from scratch, we have put a lot of thought into the infrastructure of the lab space in B221A. This lab space will house the blade trap system which is currently being assembled. The blade trap system will sit on the right 5 ft optics table shown in figure 3.1, while the lasers for the system will sit on the rear 2.5 ft optics table. The left 5 ft table will be for future expansion.[3] Fibers will be used to cross the small gap that separates these tables.

[2] B221A is an adjacent room to B221B in the basement of QNC

[3] We may end up moving the existing four-rod system to this table.

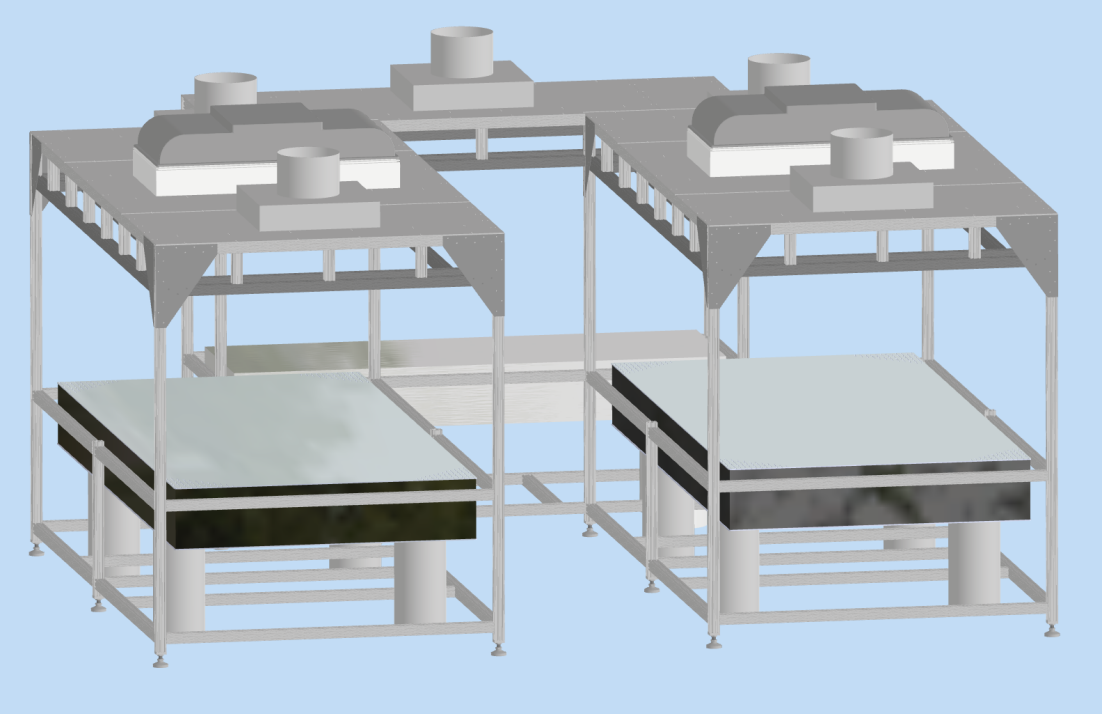


Figure 3.1: **The optics table layout for B221A.** 8020 Aluminum extrusions are used for the enclosure surrounding the tables with aluminum sheets used for the corner supports and top plates. Five hepa filters on top will connect to the air handling unit while two stand-alone hepa fan units will work as a back up if the HVAC unit is not operational. Enclosure doors are left out for clarity

3.2.1 Environmental stability

With all of this highly specialized equipment comes a great deal of heat. We estimated that a lab running two trapped ion quantum simulators could generate up to 20 kW of heat. To solve this issue, we have hired Environmental Systems Corporation (E-S-C), a company based out of Barrie, Ontario, which specializes in designing and building clean rooms. This company is designing a custom HVAC system that will stabilize the room to $\pm 0.1°C$. The HVAC unit will supply air to the five square hepa filters sitting on top of the optics table enclosure. A fabric will sit 6in below the filters in order to diffuse the air and thereby create laminar flow over the entire optics table. Two stand-alone hepa filters are placed in the center of the 5 ft enclosures and will be used as a back up if the HVAC unit were to fail.



Figure 3.2: **Water cooled amplifier box.** Thermally conductive, electrically isolating mounting tape is used to mount eight MPA-40-40 amplifiers from RF Bay to a water cooling plate to provide heat removal while keeping the amplifiers floating w.r.t. the box ground. Heat sinks are attached to the plate for back up heat removal. The front cover of the 4U Hammond box uses a 3D printed plate to electrically isolate the box from the SMA connectors.

In order to lessen the heat load on the air handling unit, water cooling will be used on affected equipment, such as amplifiers, power supplies, lasers, and cameras. Some of these systems, namely amplifiers and power supplies, only require that heat is taken away and do not require precise temperature control. For these situations, the building's water supply will be tapped into directly. Cooling blocks have been designed and integrated into the system where the heat is greatest. Currently, approximately 10 amplifiers are being used in our four-rod system, primarily to power Acousto-Optic Modulator (AOM)s and Electro-Optic Modulator (EOM)s. Due to the added capabilities of the blade trap system, the number of amplifiers required would nearly triple. To integrate this into our water cooling system, a 4U Hammond box was designed (Figure 3.2) to integrate eight four-watt amplifiers (RF Bay MPA-40-40), each with their own dedicated 24 V linear power supply

(Acopian Narrow Profile). The water cooling block separates the floating power supplies (not visible in Figure 3.2) from the amplifiers. The amplifiers attach to the block using thermally conducting, electrically insulating, double sided tape. This ensures that the amplifiers are not referenced to ground at the box in addition to being referenced at the source, thereby avoiding any potential ground loops. To isolate the box from the SMA pass-through connectors, a 3D-printed front cover was made which further insures that the RF signal is not grounded at the amplifiers. This amplifier box is currently being used with a stand-alone water chiller for the 4-rod system. It will later be integrated into the building supply once the experiment is moved into B221A.

For those systems such as lasers, AOMs and cameras that require more stable temperatures, a stand-alone precision water chiller will be used to keep the water temperature within $\pm 0.1°$C. These systems will either be cooled directly, if supported, or will sit on water cooled bread boards from Thorlabs. Enclosures will be built around these boards to further isolate these systems from the outside environment.

3.2.2 Power distribution and grounding

Much of the electronics in our lab, such as RF switches, pre-amplifiers, control boards, and voltage variable attenuates, require DC voltage(s) to function. The most common voltages are $\pm 5, \pm 15$, and $+24\ \mathrm{V_{DC}}$. Rather than bringing in a new power supply for each piece of equipment requiring these voltages, a power distribution system allows these voltages to be supplied to various points around the lab in a compact and expandable form. The first iteration of the power distribution system relied on large, high wattage linear power supplies (Acopian Gold Box), which were placed outside the lab. These DC power supplies supply voltages that are approximately 3 V higher (lower) for the positive (negative) voltages on the distribution board to account for voltage drop and linear regulators that come later. The left diagram in Figure 3.3 describes this first iteration of the DC power distribution system. From the power supplies a Festoon cable (striped yellow) would bring these voltages down to the lab where they would branch off (dotted yellow) to various locations around the lab. Distribution boards (bottom left) were placed at various locations around the lab. The boards use linear regulators to step down the voltages to the common ones mentioned earlier, as well as suppress any noise that was either picked up from the cable or left over from the power supply. These regulators have a current limit of approximately 1.5 A and since each voltage on the distribution board has two sets of linear regulators, this limits the distribution board to 3 A per voltage. This system worked well to supply a clean DC voltage, however, there was excess noise on the DC grounds due to ground loops in the system. This occurred due to the current having

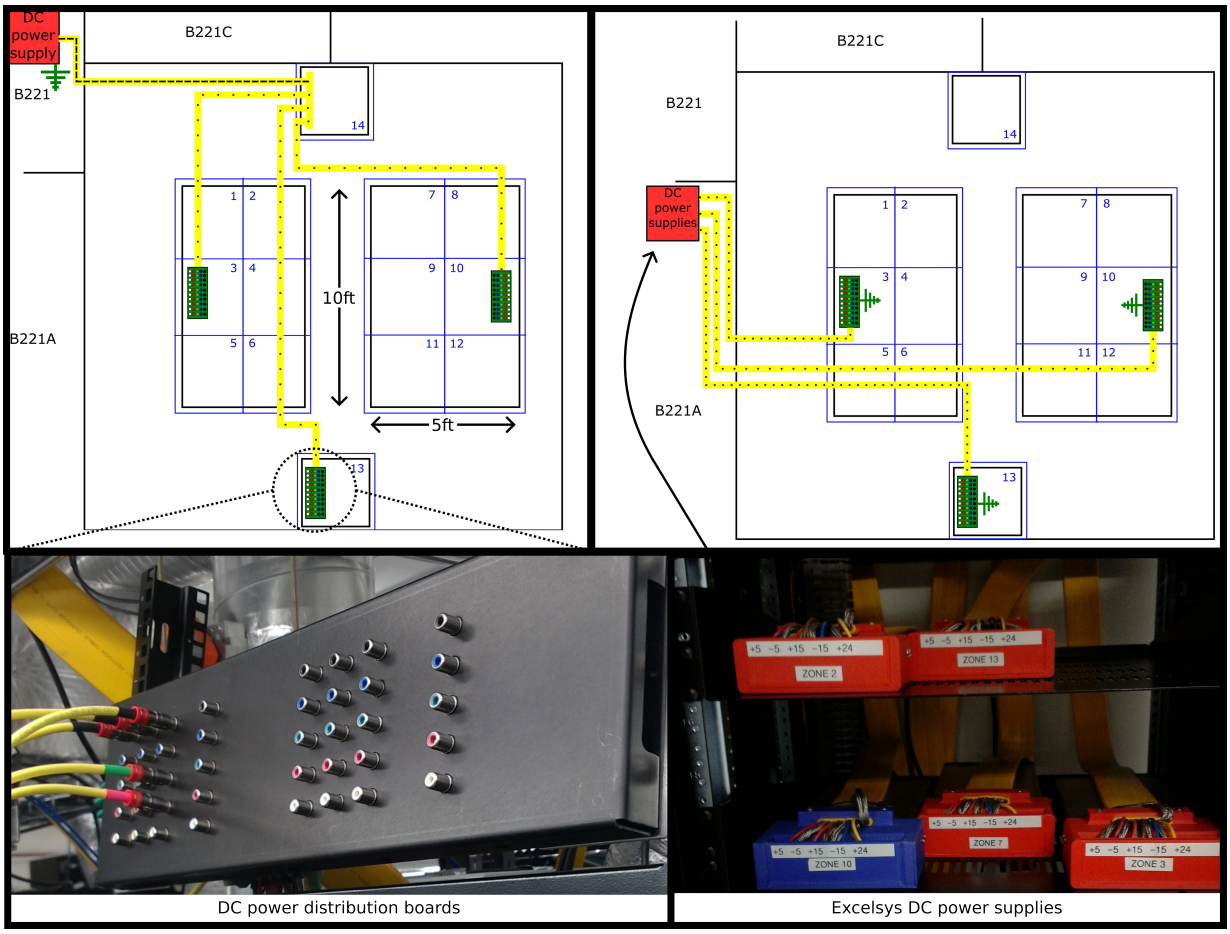


Figure 3.3: **DC power distribution.** Two layouts for the DC distribution system in QITI lab (B221B). Flexable Festoon cables (yellow) are used to bring DC voltages from power supplies to custom made distribution boards placed (bottom left) around the lab. The top left scheme follows a tree structure, where a single Festoon cable (trunk) is brought from high wattage power supply to the lab. Branches are then connected to the trunk and used to supply the distribution boards. The top right scheme uses individual power supplies for each distribution board, which requires the Festoon cable be run directly from the distribution board to the power supply (bottom right).

multiple paths back to the power supply, through the various Festoon cables or through the building ground as the power supplies had been grounded. These ground loops would cause large voltage differences, in excess of 200 mV (measured on a Fluke multi-meter), between equipment connected to the power distribution boards and various grounds in the lab, such as receptacles and optics tables. Among other things, these voltage differences are detrimental when trying to measure signals on the same scale and add a point of entry for noise to enter the system.

The new design (upper right of Figure 3.3) aimed to solve this ground loop issue. The first change was to have each distribution board be fed by its own dedicated, floating power supply. This meant that any current serving equipment powered by a distribution board would have only one path back to the power supply, through the Festoon cable (dotted yellow). Since this greatly increases the number of power supplies required, and each distribution board is limited to only supplying 3 A per voltage channel, the decision was made to try Switch Mode Power Supplies (SMPS) which are more efficient and cost effective, albeit at the expense of generating noise on the DC signal at the switching frequency (typically a few hundred kilohertz). Excelsys SMPS's were chosen due to their compact and modular design. They use a chassis (UX6) that is capable of holding six power modules (XgE), each of which can be tuned independently from 5 to 28 V to supply a maximum of 5 A to the system. These power supplies have a switching frequency of 260 kHz and a peak-to-peak ripple of 40 mV. For this reason they would require testing before implementing them into the system. The second change in the DC distribution system was to create a ground reference at the distribution board instead of at the power supply (as was the case in the old design). Since each dedicated power supply is floating, this references the DC voltages to ground while only giving one path for current to return to the power supply.

To test the switching noise from the Excelsys SMPS the frequency power spectrum was taken and is shown in Figure 3.4. On the left of Figure 3.4 is the test setup used to measure the frequency spectrum of the DC power distribution. One power module of the Excelsys power supply is connected to a distribution board using a 15 ft Festoon cable to simulate lab conditions. A high power resistor is used to simulate a load on the distribution board. A 1× oscilloscope probe was connected to a battery powered spectrum analyzer (Keysight Technologies FieldFox N9937A) to measure the spectrum. The spectrum measurement on the right of Figure 3.4 was performed on the 24 V channel of the distribution board with a 20Ω resistor. The x-axis spans frequencies from 5 kHz to 1 MHz. The y-axis measures the power in dBm contained in each frequency bandwidth (7.5 kHz). The spectrum shows that the linear regulators on the distribution board have properly suppressed the switching noise from the power supply and any other pickup from the long Festoon cable. All other

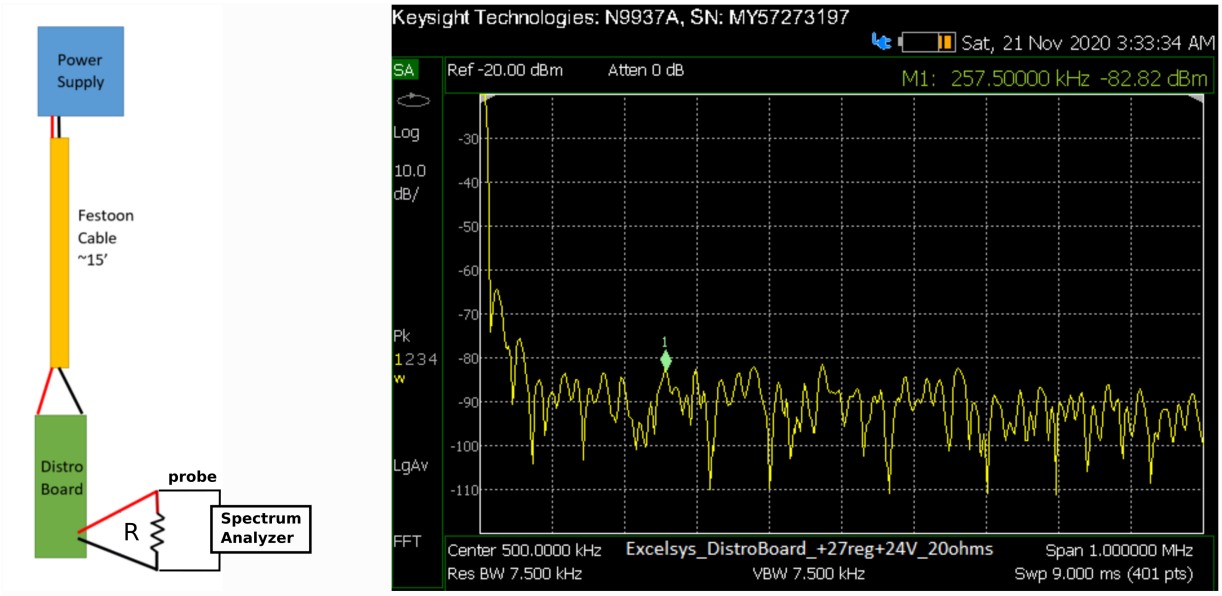


Figure 3.4: **DC power distribution spectrum measurement.** On the left is the test setup used to measure the frequency power spectrum of the DC power distribution to ensure the power supply switch frequency or any other noise is not transferred to the DC voltages. The power supply is connected to a distribution board using a 15 ft Festoon cable. A high power resistor is used to simulate lab conditions and loads. A 1× oscilloscope probe was connected to a battery powered spectrum analyzer (Keysight Technologies FieldFox N9937A, 5 kHz to 18 GHz) to measure the frequency spectrum. The spectrum measurement on the right was performed on the 24 V channel with a 20 Ω resistor. The x-axis spans frequencies from 5 kHz to 1 MHz. The y-axis measures the power in dBm contained in each frequency bandwidth (7.5 kHz). The spectrum shows that the linear regulators on the distribution board have properly suppressed the switching noise from the power supply and any other pickup from the long Festoon cable.

voltages (± 5 and ± 15) were tested in a similar way by choosing resistor values that would draw an amount of current near the maximum (1.5 A) of the linear regulators. The tests showed similar results that the linear regulators were properly suppressing the switching noise from the SMPS. The peak-to-peak voltage was measured using an oscilloscope (Rigol DS1102E) in place of the spectrum analyzer with the probe set to $10\times$ (1/10 voltage divider). Comparing the Excelsys SMPS to a linear power supply (Volteq HY3003D-3) in the same setup, there was no noticeable difference in the peak-to-peak voltage measurement between the two power supplies. These tests provide confidence that these SMPSs were not adding additional noise to the DC power. Once one of these DC distribution boards were installed using the new layout and power supply, the voltage difference between equipment connected to the power distribution boards and the nearby grounds was measured using a Fluke volt meter. Nearby grounds include the ground on receptacles, optics table and other equipment in the vicinity of the DC distribution board. Each measurement showed a voltage difference of less than 2 $\mathrm{mV_{DC}}$. This shows that the ground loops have been effectively removed in the DC power distribution system. With the infrastructure of the lab now able to support the quantum simulator, it is now possible to look at improving the robustness of the systems that are responsible for driving qubit interactions.

3.3 Lasers and Optics

While there are ion trapping systems that try to develop laser free interaction [13], many such systems (including the one discussed in this thesis) rely on lasers to create interactions between ions. Beam alignment is crucial for building a robust quantum simulator with trapped ions, as any misalignment will lead to higher fluctuations in intensity (from beam pointing instabilities). Such fluctuations would affect the strength and coherence of the laser-ion interactions. This section will focus on the build up of the 355 nm optics which drive the Raman transitions, as well as the systems responsible for maintaining their stability.

3.3.1 355nm layout

Recall from Section 2.2 that to drive the Raman transitions in our four-rod trap, the 355 nm laser must be aligned to the ions in a 'lin-perp-lin' configuration. The first attempt at this configuration had the lasers counter-propagating and perpendicular to the four rods of our trap.[4] As the beam was meant for global addressing of the ion chain (requiring near

[4]Details of this setup can be found in Anthony Vogliano Master's thesis [17]

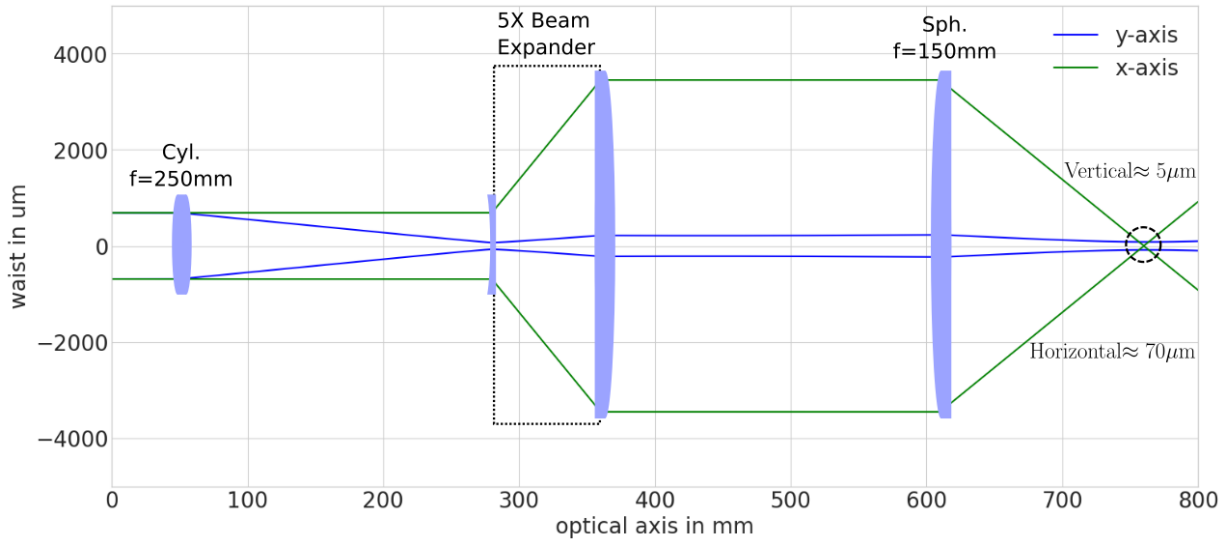


Figure 3.5: **Four-rod trap** 355 nm **optical design.** Optical design for 355 nm optics used to drive Raman transitions in the four-rod quantum simulator. The F = 250 mm cylindrical lens is placed to shrink the horizontal direction to achieve a 70 μm beam waist along the ion chain. A 5× beam expander (Edmund Optics) is paired with a F = 150 mm spherical lens to shrink the vertical beam waist to approximately 5 μm at the ions.

uniform intensity on each ion), the light from the two paths was shaped to a beam waist of 120 μm in the horizontal direction along the ion chain. To reduce the total power needed from the laser, and to have the beam fit between the rods of the trap, the beam waist in the vertical direction was squeezed to 13 μm. After many attempts to align to optics it was discovered that there were significant aberrations of the beam on the ion. This created large fluctuations which lead to short coherence times of the single qubit rotations, making the two qubit operations impossible to detect. Some of these aberrations where likely caused by imperfect alignment of the lens due to the complexity of the system. For this reason, a simpler system was designed and is shown in Figure 3.5. This system uses a single cylindrical lens (f = 250 mm), an off-the-shelf 5× beam expander from Edmund Optics (P/N 35101), and a focusing lens (f = 150 mm) to create the elliptical beam on the ions. With this setup, the beam is expected to have a horizontal beam waist of 70μm and a vertical beam waist of 5 μm. The 70 μm beam waist along the ion chain could be reduced (from 120 μm) due to the beams hitting the ion chain at a 45° angle, giving an effective increase in the horizontal beam waist of $\sqrt{2}$. With this, we insure the difference in intensity of 355 nm light falling on each ion is within a few percent. This is a requirement

for driving uniform single qubit rotations for each ion in the chain. The 5 μm vertical beam waist further reduced the total power requirement from the laser, thus decreasing the chances of degradation and damage to the optics in the system.

To allow for a future side imaging system to be installed, the 355 nm beams were shifted to a 45° angle with respect to the rods of the trap, whilst being perpendicular to each other. The optical schematic for the 355 nm system can be seen in Figure 3.6. Light from a 355 nm pulsed laser passed through a set of Polarizing Beamsplitter (PBS)'s to set the maximum amount of light sent to the four-rod experiment (typically set to between 300 mW and 1 W). After reflecting off two mirrors, the light is split using a PBS into two paths, RP1 and RP2. To precisely control the frequency and amplitude of 355 nm light on the ions, the first order beam (blue beams in fig. 3.6) of an IntaAction (ASM-2002B8) AOM is used to address the ions. To ensure that the shift in frequency (which lead to angular shifts of the first order beam) have no effect on the beam's position on the ion, the AOM is imaged onto the ions. The zeroth order beam (purple beams in fig. 3.6) is then blocked after the AOM using a D-shaped mirror and beam dump. To meet the requirements of a 'lin-perp-lin' configuration, the magnetic field which defines our quantization axis is oriented along RP1. For the polarization of RP2 to be linear and perpendicular to the quantization axis, it must be oriented vertically, or out of plane in 3.6. This then puts a requirement on the polarization of RP1 to be linear and in the plane, perpendicular to both the quantization axis and to the polarization of RP2.

The AOMs are made of Fused Silica (FS), which is suitable for high power UV light but has a first order efficiency that is polarization dependent. The optimal polarization is vertically polarized light. So, for RP2, a single half wave plate was placed before the AOM and was tuned to optimize the first order efficiency. Due to the polarization requirements at the ion, it is not necessary to have a second half wave plate after the AOM on RP2. RP1 will require a half wave plate after the AOM, however it is not shown in Figure 3.6. It should be noted that the AOM in RP2 also injects the slight shift in frequency needed to correct for the drift in repetition rate [17]. The pulse duration for our 355 nm laser is 15 ps, which corresponds to a pulse length of 4.5 mm. To drive the Raman transitions, the pulses from the two paths must overlap on the ions. After measuring the length of both paths with a ruler, mirrors M1 and M2 in fig. 3.6 are used to match the roughly 2 m long path to within a few millimeters. A retro-reflector is placed on a 1-axis translation stage and gives us the ability to align the two paths to within 100 μm of each other. For fine alignment of the beam on the ion, the last lens (L2, F=150− mm) is placed on a 3-axis ULTRAlign translation stage from Newport.

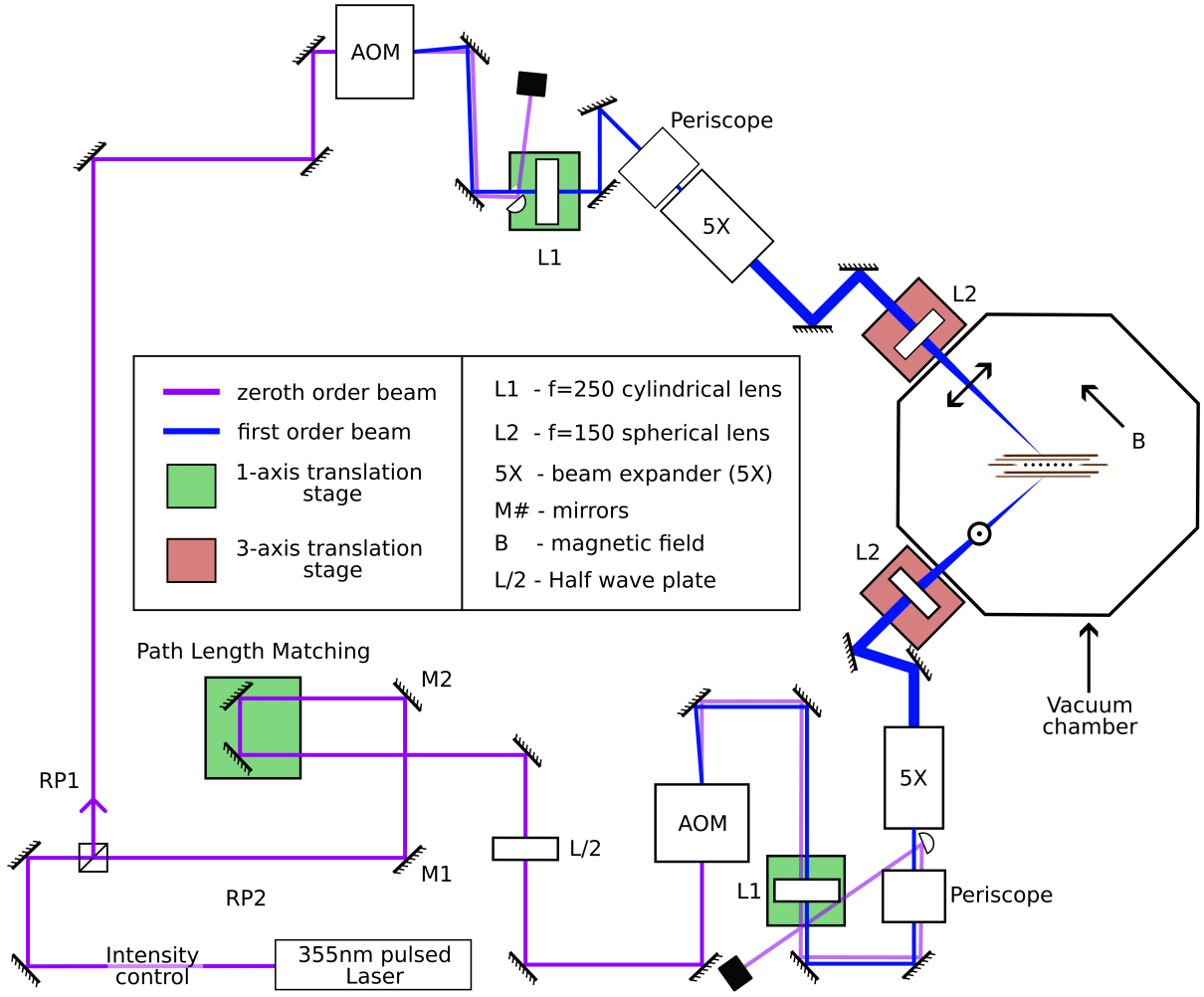


Figure 3.6: **Four-rod trap** 355 nm **optical schematic.** 355 nm light from a Paladin Advanced 355-8000 (8 W) has its intensity reduced before splitting into RP1 and RP2 using a high power Polarizing Beamsplitter Cube from Thorlabs. The beams pass through AOMs for amplitude, frequency, and phase control before being shaped by the optics that follow. The beams overlap on the ions in order to drive single qubit rotations and entangling operations. Trap electrical and mechanical connections are not shown. RP2 has a retro-reflector for path length matching to ensure that the pulse trains from each path meet at the ion simultaneously. Mirrors M1 and M2 are used to roughly match the 204(6) mm path lengths to within a few millimeters. Diagram not to scale.

3.3.2 Mechanical stability, referencing and optical control



Figure 3.7: **Optical stability and referencing.** Examples of optical stability and referencing in the 4-rod Raman system. Each element shown can be easily removed for initial alignment and is referenced to the center of the beam. Left: spherical lens (F = 150 mm) that focuses the beam on the ion. Center: cylindrical lens (F = 250 mm) on a rotation mount that creates the elliptical beam. Right: 5× beam expander rigidly mounted to a v-clamp.

While installing the 355 nm optics, several techniques and systems were implemented which greatly improved the robustness of the experiment. Figure 3.7 shows several examples of mechanically stable optical mounts used to reference the lenses to the beam path. This referencing is required as there are many times throughout the alignment process where lenses would need to be first aligned and then removed in order for the beam to be properly aligned to the subsequent lens. On the left of fig 3.7, the F = 150 mm spherical lens is fixed in a short, 1" lens tube which is then screwed onto a 1" fixed lens mount. A similar approach is taken for mounting the F = 250 mm cylindrical lens (center in fig. 3.7). Instead of screwing into a fixed mount, the cylindrical lens attaches to a 1" rotation mount. This allows the beams wide axis to be aligned with the axis of the ion chain. To mount the 5× beam expander, a large V-clamp was used which is capable of mounting up a 2" lens tube (right in fig. 3.7). This was carefully aligned so that placing the beam expander would not shift the location of the beam at a far away distance.

Due to the tight vertical beam waist, the task of achieving vertical alignment of the beam to the ion proved to be challenging. Simply turning the micrometer screw by hand would often add additional torque that would shift the beam out of alignment. To solve this, a stepper motor was attached to the translation stage using a 3D printed mount seen in Figure 3.8a. By printing gears with a ratio of approximately 3 : 1, power is transferred

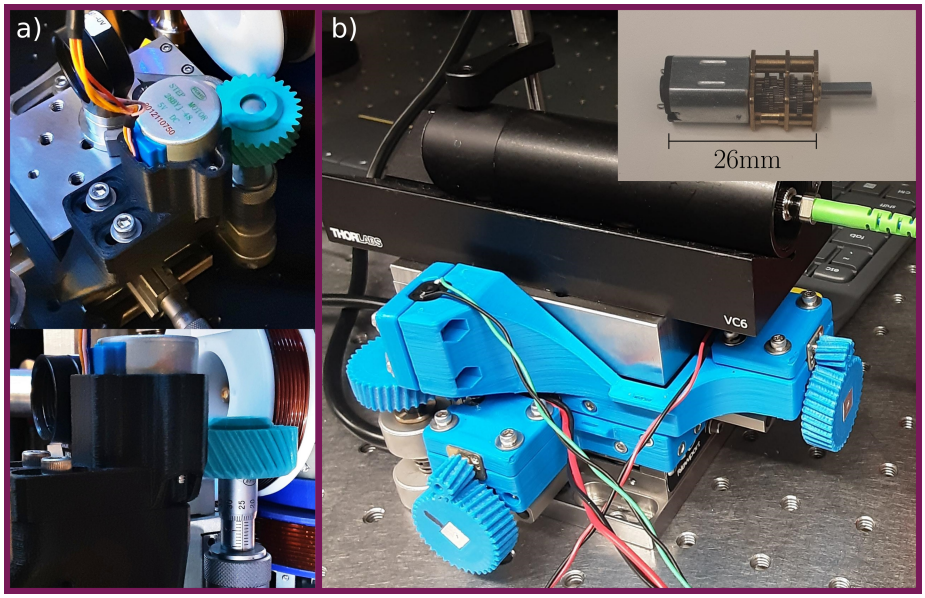


Figure 3.8: **Motorized translation stage.** Left shows the first iteration of of the motorized translation stage. This was installed on the translation stage that adjusts the vertical position of the final lens of the 4-rod Raman setup. Right shows the revised version that gives approximately 70 nm of precision on all 3 axes by using small DC motors with an approximate gear ratio of 1000 : 1 (top right).

from the stepper motor to the course knob of the micrometer screw. The first iteration with the gears used the common 3D printing material Polylactic Acid (PLA). However, these gears would bind, thus preventing smooth motion of the screw which led to difficulties with alignment. The solution was to switch to a harder 3D printing material, Polyethylene Terephthalate Glycol (PETG), which is able to withstand light abrasion. The surfaces of the gears were sanded in order to reduce friction, thereby reducing the likelihood gears would bind, resulting in more accurate alignment. By sending many small steps to the stepper motor and tracking the dials of the micrometer screw, I estimated the vertical resolution to be roughly 0.5 μm. Due to the ease of vertically aligning the 355 nm beams to the ion, it is desirable to incorporate this control into the blade trap system. However, this would require more resolution due to the 1 μm beam waist of the 355 nm beam in that system. In Figure 3.8b the second iteration of the motorized translation stage can be seen. By incorporating small DC motors (upper right of Figure 3.8) with an advertised gear ratio of 1000 : 1, and a finer thread adjustment screw (up to 254 tpi), a resolution of approximately 70 nm per step was reached. By slightly redesigning the mounting of

the motors to fit below the top level of the translation stage, we plan to incorporate this control into multiple systems in the blade trap.

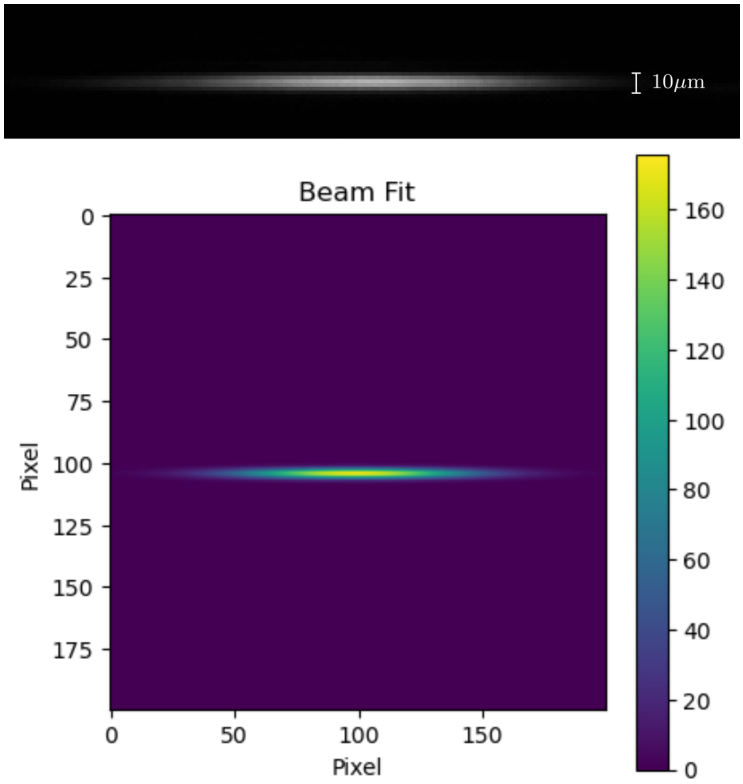


Figure 3.9: 355 nm **beam image.** Top is the image of the RP2 355 nm beam at the ions captured using a FLIR camera (BFS-PGE-120S4M-CS) with a pixel size of 1.85 μm $\times$ 1.85 μm. Bottom is a Gaussian fit of the image and gives a beam waist of 3 μm in the vertical direction and 65 μm along the horizontal. Linear colour scale indicates the irradiance of the beam (arbitrary units).

3.3.3 Beam alignment

The first stage in alignment was to center the beam on each of the lenses. This provides the maximum range and least chance of clipping for the later stages of alignment. A pinhole aligning tool was used to center the beam on the spherical and cylindrical lenses. By using the axial translation of the stages, the beam could also be aligned perpendicular to the

surface of the lens. To align the beam expander, an iris was placed at the entrance. By closing the iris and ensuring the outgoing beam reduced in size symmetrically, the beam could be centered on the initial surface of the beam expanded. The beam could be aligned axially by closing the iris and placing a slightly larger pinhole on the last lens of the beam expander. Several iterations were required to verify that the beam's position did not shift when installing the 5× beam expander in the beam path. The alignment of the beam to the path length matching translation stage was critical because the final tuning is done using the ion signal. The signals used when matching the length of the two paths can be mistaken for changes due to the intensity of light falling on the ion (due to the beam position changing) if the path length matching stage is not properly aligned. By monitoring the beams nearly 2 m away, the beam was aligned until there was no perceivable shift in position (by eye) when moving the stage through its range of motion. By placing pinholes on the view ports of the vacuum chamber, the beam could be centered and leveled through the 4-rod trap where the ions sit. The shadows of the needles were used to verify that the beam was centered with the trap in the horizontal direction. Once this alignment was complete, all lenses were placed and the beam waist at the ion's position was measured on an FLIR camera (fig. 3.9) with a pixel size of 1.85 μm × 1.85 μm. By performing a 2D tilt compensated Gaussian fit, the beam waist was found to be 3 μm in the vertical direction and 65 μm along the horizontal direction.

In this setup, Raman transitions require the 355 nm beam from both paths to be hitting the ion. This requirement demands a way to align just a single beam. Luckily, there is a rather simple way of detecting very weak signatures of 355 nm light in the form of a microwave Ramsey experiment. A Ramsey experiment consists of the following: prepare the ion in the $|\downarrow\rangle$ state, apply a $\pi/2$ rotation about y (x), wait for a time t, apply another $\pi/2$ rotation about y (x), and measure the resulting state of the ion. This process begins by precisely calibrating the frequency of the microwave horn to the qubit frequency. This allows the qubit to be driven from $|\downarrow\rangle$ to $|\uparrow\rangle$ at a rate of about 10 μs. By detuning the microwave frequency from the qubit frequency by an amount δ (usually ten kilohertz to start), and scanning the wait time t, we see flopping from $|\downarrow\rangle$ to $|\uparrow\rangle$ at a rate equal to the detuning (δ). If we now turn on our 355 nm light from one of the paths, and some of the light is hitting the ion, it will induce AC Stark shift (AC in Figure 3.10) which has the effect of changing the qubit frequency [18]. The increase in qubit frequency is proportional to the intensity of light the ion is seeing. As the center of the beam (which has a higher intensity) moves closer to the ion, the rate of oscillations will increase due to the increase in the detuning (δ' in Figure 3.10). Since AC Stark shift is maximized for pure σ_+ or σ_- polarization, a $L/4$ waveplate could be added to RP1 to achieve maximal signal strength when the magnetic field is parallel to RP1. RP2, on the other hand, will not see any

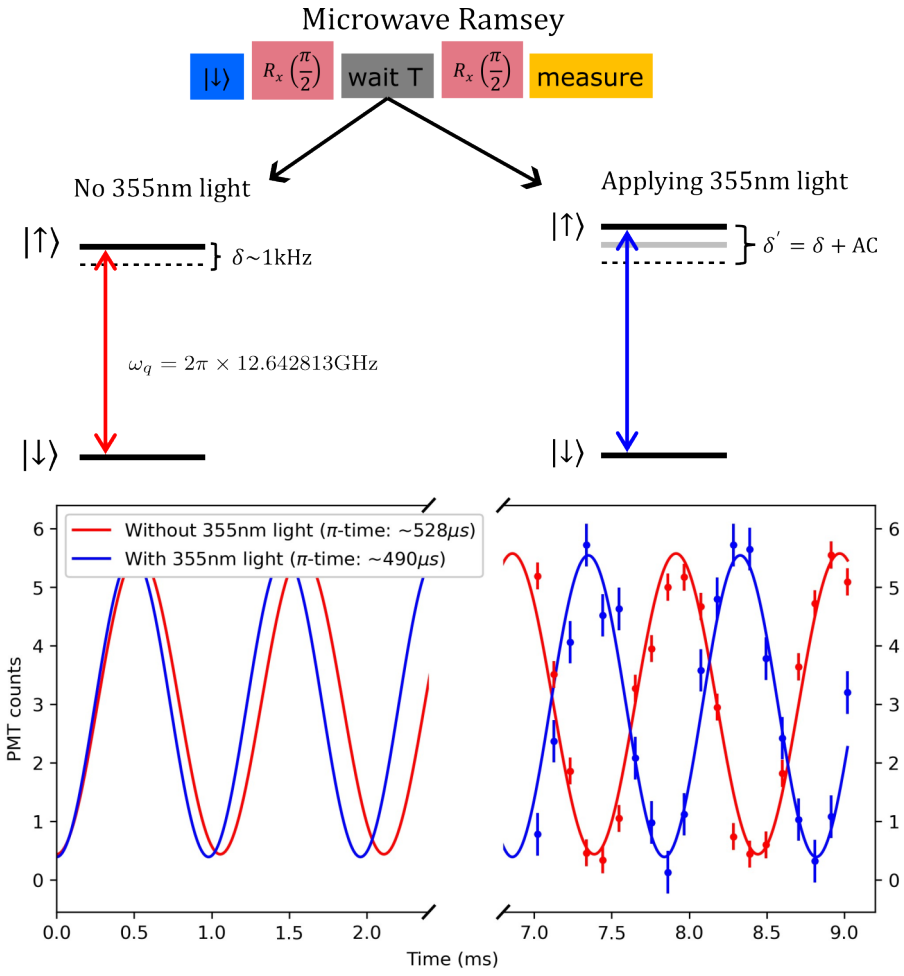


Figure 3.10: 355 nm **alignment using off-resonant microwave Ramsey interferometry.** Top shows the experimental sequence of a Microwave Ramsey experiment. The energy level diagrams show how applying 355 nm during the wait time (t) light has the effect of increasing the effective detuning (δ') of the microwave frequency from the qubit frequency. The plot shows the detection counts measured on a PMT. 20 Measurements where made for wait times (t) between 7 and 9 ms. Red shows a microwave Ramsey with no 355 nm light on the ions. Blue shows the same Ramsey experiment with 355 nm light aligned to the ions. Error bars (for both red and blue) represent the standard deviation of the bright state detection florescence for the 20 data points in each experiment. Fit function: $A\sin^2\left(\frac{\pi t}{2T}\right) + \text{offset}$ where $\pi-\text{time} = T$.

imbalance of $\sigma_{\pm}$ unless the magnetic field direction is changed. Orienting the magnetic field along the ion chain allows for a visible AC Stark shift signal from both Raman paths. Figure 3.10 shows the effect of applying 355 nm light to the ion after some alignment has taken place. The orange data shows the Ramsey oscillations with $\delta \approx 1$ kHz. The light blue data shows the same Ramsey experiment with the 355 nm light aligned to the ion. Figure 3.11 shows the effects of setting $\delta = 0$ and of applying 355 nm light, both of which provide an easy way to measure exactly how much AC Stark shift is induced on the ion by measuring the rate of flopping from the $|\uparrow\rangle$ to the $|\downarrow\rangle$ state. RP1 is able to induce over 700 Hz of AC Stark shift while RP2 was able to reach just over 300 Hz by sending approximately 150 mW of optical power to the ion. This discrepancy comes from the inability of RP2 to produce pure $\sigma_{\pm}$ polarization on the ion.

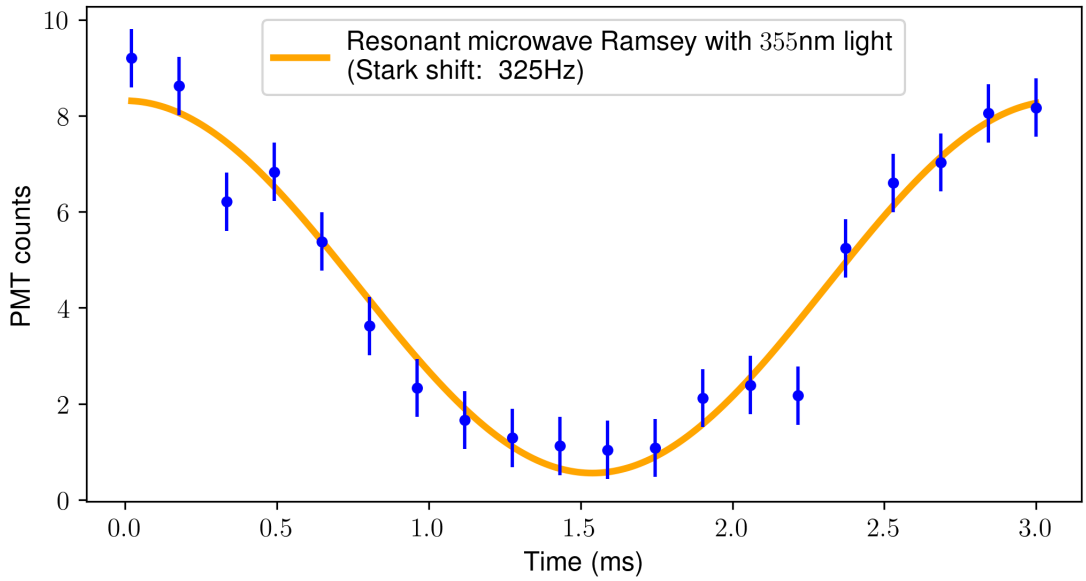


Figure 3.11: **Resonant microwave Ramsey with** 355 nm **light.** Data points (blue) are the average detection counts measured on a PMT (100 experimental repetitions) while performing a resonant microwave Ramsey experiment with the 355 nm laser shining on the ions through RP2. Error bars represent the standard deviation of the bright state detection florescence for the 20 data points in the experiment. These oscillations are due to the AC Stark shift from the 355 nm light and are measured to be on the order of $\omega/2\pi = 300$ Hz while sending approximately 150 mW of optical power. Fit function: $A\cos^2(\omega t) + \text{offset}$.

Now that the beams are hitting the ion, a carrier Raman transition (seen in Figure 3.13)

can be directly driven for fine alignment of the beam and path length matching. The initial steps of this are slightly more complicated since, in order to see Raman transitions, we need to have the path lengths matched to within 4 mm for the pulses to overlap at the ion. In addition, the beams in the two paths must have a frequency difference such that they drive the carrier transition. The first hurdle can be solved by having multiple people carefully measure the paths to confirm they are within a few millimeters of each other. The length of RP1 was found to be 204(6) mm. The second relies on the fact that carrier transition is quite broad at high optical powers. It is therefore possible to set a large flopping rate (a few milliseconds) and scan the frequency of one AOM (around a value estimated through calculations) in order to see excitations to the $|\uparrow\rangle$ state. Once a peak is observed, the AOM can be set to that frequency in order to obtain a proper measure of the carrier flopping rate. Repeating this once more produces an accurate frequency measurement of the carrier transition. Since the flopping rate is proportional to the intensity of the light on the ion, the flopping rate can be used as a faster signature of beam alignment. After optimizing the position so that the ion sits at the focus of both 355 nm beams, and optimizing the path length matching translation stage (again using the flopping rate), a Raman carrier rate (π-time) of 1.5 μs has been achieved by addressing the ion with approximately 150 mW of power through both 355 nm paths. Figure 3.13 shows an example of carrier Raman oscillations but with a slightly slower π-time. It should be noted that, in order to achieve this high flopping rate, I had to develop the motorized vertical knob from the preceding section as manual adjustment proved to be unreliable for the precise adjustment needed near the beam's focus.

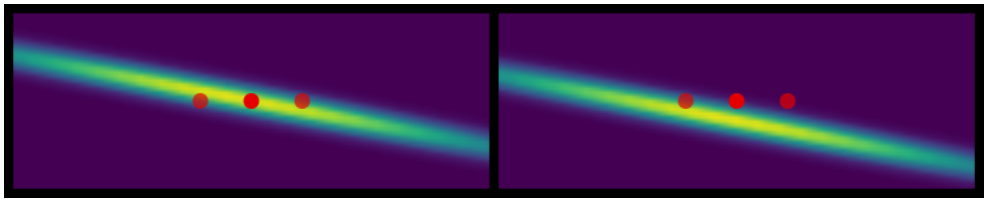


Figure 3.12: **Cylindrical lens alignment.** The left shows the 355 nm beam centered on the ions. In this configuration, moving the ions left and right of center would show a symmetrical decrease in Rabi frequency, regardless of the alignment of the horizontal beam waist to the ion chain. The right shows the 355 nm beam displaced from the center ion. In this case, moving the ions left and right of center would show a symmetrical Rabi frequency only in the case where the horizontal beam waist is aligned to the ion chain. Ions not to scale.

The final knob to touch is the rotation of the cylindrical lens to align the wide beam axis

to the ion chain. This insures that each individual ion sees nearly the same beam intensity (when properly aligned) which is needed for experiments that require uniform two qubit interactions on many ions. This axis can be aligned by using a single ion and adjusting its horizontal position by varying the voltage on the needle electrodes. If this were to be done with the beam centered on the ion as seen on the left of Figure 3.12, there would be a symmetric reduction in carrier flopping rate when shifting left and right of center. For this reason, the beam is first offset in the vertical direction to break the symmetry of the right and left sides. Since turning the cylindrical lens can also introduce a positional shift of the beam, this process was iterated over (realigning to center and then offsetting) until the symmetry of the flopping rate was restored. With the Raman laser aligned to the ions, I have created a more robust system that improves on the previous system's capacity to run complex quantum simulations.

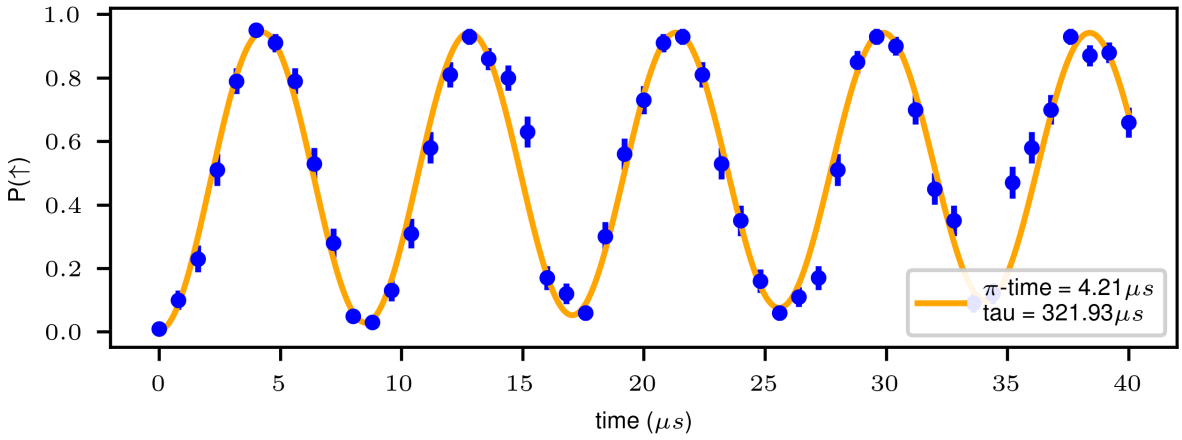


Figure 3.13: **Raman carrier flopping.** Y-axis displays the probability of finding the qubit in the $|\uparrow\rangle$ state (normalized by performing a microwave π rotation to account for fluctuations in the detection laser's intensity). X-axis shows the amount of time that the 355 nm lasers were applied to the ion while addressing the carrier transition. Error bars show the standard error over 100 experimental repetitions. Fit function: $\cos^2(\omega x)\left(Ae^{-x/\tau} + B(1 - e^{-x/\tau})\right)$ where $\pi-\text{time} = \pi/(2\omega)$.

Recall from Equation 2.2 that the Raman carrier transition is related to the Rabi frequencies from the two laser beams, Ω_1 and Ω_2. These Rabi frequencies are proportional to the amplitude of the electric field and thus are related to the intensity of 355 nm light on the ions (from RP1 and RP2). Since the ions are not perfect point particles, and on the atomic scale the beam is not perfectly stable, the intensity of light that the ion sees

fluctuates. If the beam is centered on the ion, these fluctuations will be minimized. If, however, the ion is seeing the edge of the Gaussian beam, the intensity of fluctuations will be larger, potentially leading to decoherence in the flopping from the $|\downarrow\rangle$ to $|\uparrow\rangle$ state. Figure 3.13 shows the probability of finding the qubit (ion) in the $|\uparrow\rangle$ state. The x-axis denotes the amount of time the 355 nm beams were applied to the ion to drive carrier transitions. Figure 3.13 shows that the decay of the carrier Raman transitions (tau (τ) $\approx$ 320 μs) is much longer than the time for a single transition from $|\downarrow\rangle$ to $|\uparrow\rangle$ (π-time $\approx$ 4.2 μs). This gives confidence that the two 355 nm beams are centered on the ion with reasonable stability.

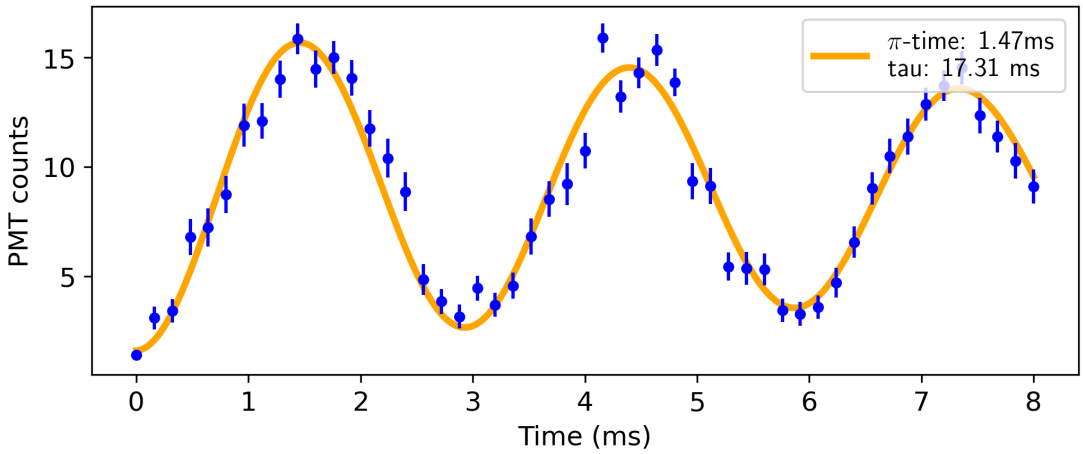


Figure 3.14: **Ion fluorescence while applying a MS scheme.** Y-axis displays PMT counts for a detection time of 400 μs while the x-axis shows the amount of time the MS laser scheme was applied to the ions. Error bars show the standard error over 100 experimental repetitions.
Fit function: $\sin^2(\omega x)\left(Ae^{-x/\tau} + B(1 - e^{-x/\tau})\right)$ where $\pi-\text{time} = \pi/(2\omega)$.

3.3.4 Two-qubit entangling

The ability to entangle qubits is an essential tool for the four-rod trap quantum simulator. The MS scheme requires the stability of many components, including trap frequency, laser frequency, and intensity of 355 nm light on the ion, and thus provides a good bench mark for this system. Instabilities in any of these systems can potentially lead to decoherence in the flopping of $|\downarrow\downarrow\rangle$ to $|\uparrow\uparrow\rangle$. Figure 3.14 shows the first few flops of a pair of ions while

applying the 355 nm beams in a MS scheme. It is clear that the system is stable within the first few flops. This suggests a robust beam delivery of the 355 nm light to the ions. With the Raman system deployed and the ability to reliably entangle qubits, it has been possible to run a multitude of quantum simulations, one of which includes many-body spin cooling [12] [1]. It has also lead to the verification of a new way to produce xy-type spin interactions[5], which were formally thought to be very challenging to implement or only applicable in certain specific simulations [19].

3.4 Reaching XHV

Until now we have limited ourselves with dealing with simulations of six or fewer ions on the four-rod trap. This is in large part due to the lack of NA from the imaging system and lower trap frequency, both axial and radial. The blade trap system improves on these systems, but as system size starts to increase, the vacuum pressures would become a limiting factor. This is due to the collision rate from the background gasses left in the chamber. These collisions cause a decrease in ion lifetimes and disrupt experiments when ions get kicked from the trap. The rate of these collisions can be calculated from the mean free path length which is a direct measure of the pressure around the ions. To reach a background collision rate on the order of an hour, pressures are required to be in the mid to high 10^{-13} mbar.

Many of the components used in this vacuum system have already been shown to reach the pressures required for these experiments. The stainless steel that makes up the chamber and some internal components can be baked at high temperatures to reduce the out-gassing rate of hydrogen defused into the bulk material. Similarly, the Kapton wires can be heated to remove the water in the bulk material [20]. One lesser known material[6] used in the system was the ceramic developed by Precision Ceramics called Shapal. This ceramic was used to make the blade electrode holder as it has superior RF heating rate compared to the more commonly used ceramic Macor while still retaining machinability. With some research on the out-gassing behaviours of Shapal, the decision was made to test it in this system to see if it could achieve the XHV pressures that are required for the blade trap [21].

After meticulously preparing the vacuum chamber[7] and then baking it at 200°C for a

[5] $H = \sum_{ij} \left(J_{ij}^x \sigma_x^i \sigma_x^j + J_{ij}^y \sigma_y^i \sigma_y^j \right)$

[6] lesser known in the ion trapping community, at least

[7] Again, these details can be found in Sainath Motlakunta PhD thesis [1] and later in Nikhil Kotibhaskar's PhD thesis

few days and then allowing it to return to room temperature, the empty chamber was able to reach pressures close to 8×10^{-13} mbar. In contrast, when the chamber contained a test piece of Shapal that was roughly the size of the blade holder, it could not reach pressures below 1×10^{-9} mbar. The research on Shapal's vacuum capabilities suggests that water vapour trapped during the forming process was the dominate contribution to the outgassing rates [21]. With insight from this research, the test piece was baked in a MTI 100 mm quartz tube furnace at 400°C under vacuum for one day. After this preparation, the blade trap vacuum chamber was able to reach base pressures an order of magnitude lower with the Shapal piece inside ($\approx 1 \times 10^{-10}$ mbar). While great, this would still limit the achieved pressures to those almost 3 orders of magnitude higher than the pressures required for large chain quantum simulations. With some back-of-the-envelope calculations, it is estimated that leaving the blade holder in the tube furnace for 10 days at about twice the temperature would lead to base pressure in our chamber of about 10^{-13} mbar. Based on these calculations, the blade holder was baked at 900°C, as this is a few hundred degrees below the glass transition for Shapal. As the flanges currently available on the tube furnace were not meant to sustain high vacuum, a large Edwards turbo pump was connected in order to compensate for any leaks coming from the flanges. The temperature was increased slowly to prevent the Shapal from cracking due to internal stresses. The ramp profile was set manually on the tube furnace in one day intervals to allow for changes in the profile during the baking. The ramping profile was as follows:

- Room temperature to 900°C in 36 hours
- 900°C for 288 hours (12 days) in 24 hour increments
- 900°C to 450°C in 24 hours
- 450°C for 24 hours
- 450°C to room temperature in 24 hours

In the end, the Shapal sustained 900°C for 12 days at a pressure of about 5×10^{-5} mbar when measured near the holder. With this preparation, our blade trap vacuum chamber has successfully reached pressures of approximately 9×10^{-13} mbar with the blade holder inside.[8] These pressure measurements were conducted using an ion gauge (Agilent UHV-24p) with an x-ray limit of 5×10^{-12} Torr. When aligning the blades, it was determined

[8]The vacuum system comprised of a single activated SEAS Z1000 getter pump inside an 8" nipple and a Gamma vacuum 75L/s ion pump. More details on the preparation and setup can be found in Sainath Motlakunta's PhD thesis.[1]

that the blade holder itself had a few dimensional inaccuracies which prevented the blades from being symmetrical, which is a requirement for low ion heating rates [17]. Luckily, there was a spare holder that satisfied the dimensional requirements. After repeating the process in the tube furnace, pressures again fell to the high 10^{-13} mbar inside the vacuum chamber. Having minimized the out-gassing of the blade holder, I have now created a more robust environment for performing large chain quantum simulations.

3.5 Summary and Discussion

As quantum simulators become more complex, increasingly robust systems will be required in order to support them. By designing and engineering environmental systems such as an optics table enclosure and water cooled amplifiers, I have helped create a stable environment for the blade trap and four-rod trap quantum simulator. I re-designed our existing DC power distribution and grounding system to maintain a clean supply of voltages to our experiment while reducing ground loops that can inject noise into this simulator. By carefully planning and aligning the 355 nm optics in RP2, I was able to drive entangling operations between two ions in the four-rod trap system. Incorporating 3D printed structures and small DC stepper motors, I created an accessible and reliable way to align the 355 nm beam in the vertical direction to the ions. By improving the design, I was able to achieve resolution of about 70 nm in all three axes. To reduce the background scattering events in a greater-than-30 qubit trapped ion quantum simulator, I have successfully prepared the Shapal blade holder to reach vacuum pressures of 9×10^{-13} mbar. The development of these robust systems provides a reliable foundation for further experiments, and improves the capabilities of the trapped ion quantum simulator.

To support two trapped ion quantum simulators, a new lab will require extensive infrastructure. While much has been done already on this front, one area of focus going forward should be to improve the back-up power supply. These are emergency plugs that will be fed by a generator in the case of a power outage. This would allow anyone working in the lab to safely shut down the lasers and computers in the case of a power outage. To build on the DC power distribution system, a high current version of the board can be implemented to supply power to equipment such as Raspberry Pi's and DS Instruments RF sources, both of which can easily overload the linear regulators on the distribution boards. This will lessen the need for bulky and potentially noisy power bricks around the lab. This would require the power supply to be placed in the lab. For this reason, further testing should be done to characterize the emitted switching noise and reduce it if necessary.

Chapter 4

Blade trap imaging

In this chapter I will discuss the design, development, and testing of the primary imaging system for the blade trap in hopes of reaching high state detection fidelity with detection times on the order of 20 μs.

- **Section 4.1:** I will motivate the requirements of fast detection times during mid-circuit measurement by summarizing a paper I co-authored [12]. This section also serves as an introduction for the chapter.
- **Section: 4.2:** I will revisit the physics of state detection in $^{171}Yb^{+}$. I will primarily be following the work done by Rachel Noek [22] with contributions from Sainath Motlakunta [12].
- **Section 4.3:** Here I will discus the experimental requirements for the blade trap system and describe the optical layout for the full blade trap imaging system.
- **Section 4.4:** I will investigate the design requirements for high fidelity mid-circuit measurement. I start by breaking down the system efficiencies for the blade trap imaging system in order to understand the variables that are able to be controlled (4.4.1). In 4.4.2, I evaluate the effects that sharing an objective with a classical Raman beam has on single photon detection. I then simulate our system and determine that, with enough engineering, high fidelity, fast, mid-circuit measurement should be possible with a PMT detector in the blade trap system.
- **Section 4.5:** I start by detailing the designs for the mounting of the 0.5 NA objective used in the imaging system (4.5.1). I then give a brief introduction to the

optical simulating software Zemax, which should help new users conquer the steep learning curve of optical engineering (4.5.2). I then evaluate the optical system that I engineered for the primary imaging of the blade trap. I'd like to thank Chung-You Shih and Sakshee Samir Patil for their insights into simulating optical systems with Zemax.

- **Section 4.6:** Here, I describe the steps that were taken to align the high NA imaging system and the steps taken to test the performance of the doublet that was engineered in Section 4.5.2.

- **Section 4.7:** I discuss the performance of the system and outline some of the factors which suggest that alignment in the blade trap system will be easier than the challenges faced in the test setup described in Section 4.6. I detail an improved strategy for aligning the high NA imaging system and give further optimizations to the current optical design.

4.1 State of the art

To convey the importance of state detection, and to motivate the work in the subsequent sections, I will start by summarizing a recent paper from our group, for which I was a co-author, entitled 'Preserving a qubit during adjacent measurements at a few micrometers distance' [12]. Up until now, individual addressing of an ion (within a chain) with incoherent operations (such as measurement or state reset), without decohering the state of the neighbouring ions was a difficult endeavor. Demonstrations of this would require either complex traps to shuttle (move) the ions apart, or the ability to trap and address ions of multiple species or isotopes. These techniques were needed primarily to shield the ions in the system that were not being measured (asset qubits) from the light addressing the ions of interest (process qubits). To perform these state measurements or resets in-situ was previously thought to be intractable due to the leaked light from the addressing beam. Even if this could be overcome, it was thought that the scattered photons from the process qubit would decohere the neighbouring asset qubit too quickly, thereby leading to low preservation fidelity (the fidelity of preserving the neighbouring qubit state while addressing the process qubit). Because we have a novel way of correcting for optical aberrations in our addressing system in the form of a DMD [10], we decided to challenge these preconceived notions.

By carefully calibrating the aberrations using our DMD in the four-rod system, and with the ion as a point source sensor, we were able to limit the intensity crosstalk between the

laser beam and the neighbouring ion to below 8×10^{-5} using a probe beam of $I/I_{sat} = 1.25$.[1] With this, we showed that not only is it possible to achieve high fidelity in-situ mid-circuit measurement or state reset ($> 99.6\%$ and $> 99.9\%$ preservation fidelity, respectively), but also that the decohering effects from inter-ion scattering are at least an order of magnitude lower than previously thought. The discrepancy in the measurement to state reset fidelity is primarily due to the difference in process time. Roughly speaking, the longer the light needs to shine on the process qubit, the more likely it will decohere the state of the neighbour ion. Since state reset does not rely on the ability to collect (and then detect) the scattered photons (from the process ion), this process is complete in just a few microseconds. State detection, on the other hand, has a process time that depends on the efficiency of the detection system. To reach the high preservation fidelity that was quoted for mid-circuit measurement, there is an assumed process time of 11 μs [23]. This process time has been shown to be possible in the trapped ions platform. However, it requires a state-of-the-art detection system, using an Superconducting Nanowire Single-Photon Detector (SNSPD) with near zero dark counts and high quantum efficiencies ($> 70\%$) [23]. To clarify my choice of words, the term process time refers to the average time that the light is shone on the ions. For state reset, this value is constant and is calibrated by measuring the pumping rate from the $|\uparrow\rangle$ to the $|\downarrow\rangle$ state. For detection, this time can differ from the detection time, if a system has the ability to time tag photons (more accurately, time tag the counts from the detector). With this ability, the detection light can be shut off as soon as a set number of photons in a given time (threshold) is received. With this implemented into a detection process, the expected process times are approximately half that of detection times [23]. This gives the requirement of reaching detection times on the order of 20 μs to preserve the neighbouring ions during mid-cuircut measurement.

Over the past five years, the team at QITI lab has been developing the blade trap system to reach what may be the lowest pressures on a room temperature ion trap, individually address a chain of up to 30 ions with state detection or reset, and drive two qubit transitions between arbitrary ions in this chain. A quantum simulator such as this requires a robust imaging system to ensure that it remains relevant and cutting edge for years to come. This section will discuss the development of this system in the hopes of reaching process times that are comparable with the 11 μs system [23], while sticking to conventional means of detection (PMT). These capabilities will open many doors into the world of quantum simulation, including the ability to simulate measurement induced phase transitions [6].

[1] I/I_{sat} is the ratio of the applied laser intensity to the saturation intensity for the transition under study.

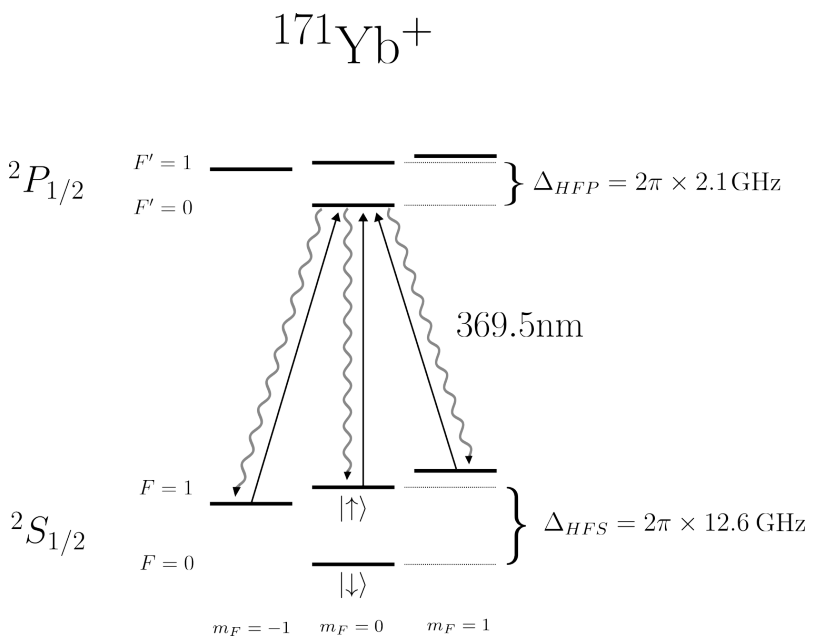


Figure 4.1: ^{171}Yb$^+$ **detection transition**. A 369.5 nm laser is turned to the cycling transition of the $F = 1$ to $F' = 0$ state. With some probability, the photons emitted when the atom decays will be detected by a PMT or camera. Δ_{HFS} and Δ_{HFP} are the hyper-fine splittings of the S and P manifold, respectively.

4.2 Detection physics

To understand how we plan to reach detection times on the order of 20 μs/ (thus process times ≈ 10 μs), I will explain the physics of detecting ^{171}Yb$^+$ in more detail. Recall from chapter 2 where we defined the qubit states $|\downarrow\rangle$ and $|\uparrow\rangle$ using the two hyper-fine levels of the ^{2}S$_{1/2}$ manifold $|F = 0\rangle$ and $|F = 1, m_F = 0\rangle$, respectively. To detect which state the ion is in, the 369 nm laser is applied to the ion with a frequency that is tuned to be on resonance with the ^{2}S$_{1/2}$ $|F = 1\rangle$ to ^{2}P$_{1/2}$ $|F' = 0\rangle$ as seen in Figure 4.1.[2] If the atom is in the $|\uparrow\rangle$ state, there is a probability of it being excited to the $|F' = 0\rangle$ state. Once in this excited state, the atom will emit a photon, thereby decaying to one of three levels: the $|F = 1, m_F = -1\rangle$, $|F = 1, m_F = 0\rangle$ or $|F = 1, m_F = +1\rangle$. If the laser has all three polarizations (σ_+, π and σ_-), this process of exciting the atom and then emitting a photon will continue. It is these photons that are collected to determine the state of the qubit.

[2]From here on I will refer to the hyper-fine state in the ^{2}S$_{1/2}$ manifold as non-primed, and states in the ^{2}P$_{1/2}$ as primed.

Since the $|F' = 0\rangle$ to $|F = 0\rangle$ transition is forbidden, a cycling transition is formed which allows the state of the ion to be determined. So if a photon is (not) collected, we determine the ion was most likely in state $|\uparrow\rangle$ ($|\downarrow\rangle$).

Now that I have explained the process at which the ion's state is detected, I will take a closer look at the physics that drives this process. With the ion in either the $|\downarrow\rangle$ or $|\uparrow\rangle$ state, there are three processes to consider: the scattering rate of the $|\uparrow\rangle$ state (R) described above, the dark state pumping rate (R_d), and the bright state pumping rate (R_b). Dark state pumping occurs when an ion in the $|F = 1\rangle$ state off-resonantly excites to the $|F' = 1\rangle$ state and then decays to the $|\downarrow\rangle$ state. If dark state pumping occurs before enough photons have been collected (in order to determine the ion was in the $|\uparrow\rangle$ state), the ion will be wrongly categorized as being in the $|\downarrow\rangle$ state. Bright state pumping follows a similar process where an ion that is initially in the $|\downarrow\rangle$ state is off-resonantly excited to the $|F' = 1\rangle$ state and decays to the $|F = 1\rangle$ state. An ion initially in the $|\downarrow\rangle$ state can then start scattering photons which, if collected by the detection system, will lead to being wrongly categorized as being in the $|\uparrow\rangle$ state.

To fully capture the physics of these scattering rates, the coherent dark state must be taken into account. This state is easily understood by considering an ion in the $|\uparrow\rangle$ state and only applying π polarized light. Once the ion excites to the $|F' = 0\rangle$ state and decays to either the $|F = 1, m_F = -1\rangle$ or $|F = 1, m_F = +1\rangle$ state, it will no longer continue its cycling transition (ignoring any off-resonant excitations). It turns out that even when applying all three polarizations, there exists a superposition of the three $|F = 1\rangle$ states that leads to the same effect where the ion ceases to emit photons. In this superposition, the ion is said to be in a coherent dark state. This effect can be minimized by applying a magnetic field on the ion, thereby inducing a Zeeman shift in the different m_F levels to break the degeneracy, which then leads to a time-dependent coherent dark state polarization [24]. The following scattering rates have assumed an optimal Zeeman splitting of $\delta = \Omega/2$ which comes from balancing δ to reduce coherent dark state population while not being too off-resonant to keep Ω large.

With the coherent dark state effect taken into account, we can obtain the scattering rates of the different transitions and detection probabilities. The optimal scattering rate of the $|\uparrow\rangle$ state is given by:

$$R_{\text{opt}} = \left(\frac{1}{3}\right)\left(\frac{\Gamma}{2}\right)\frac{s_0}{1 + \frac{2}{3}s_0 + \left(\frac{2\Delta}{\Gamma}\right)^2} \tag{4.1}$$

Here, $\Gamma = 2\pi \times 19.6$ MHz is the line width of the $^2\text{P}_{1/2}$ state, Δ is the detuning of the laser's frequency from the $|F = 1, m_F = 0\rangle$ to $|F = 0, m_F = 0\rangle$ cycling transition, and $s_0 = 6\Omega^2/\Gamma^2$

is the on-resonant saturation parameter with Rabi frequency Ω. The dark state pumping rate for an ion in the $|F = 1\rangle$ state is given by:

$$R_{\mathrm{d}} \approx \left(\frac{2}{3}\right)\left(\frac{1}{3}\right)\left(\frac{\Gamma}{2}\right)\left(\frac{2\Omega^2}{\Gamma^2}\right)\left(\frac{\Gamma}{2\Delta_{HFP}}\right)^2 \tag{4.2}$$

where the hyper-fine splitting of the $^2\mathrm{P}_{1/2}$ manifold is given by $\Delta_{HFP} = 2\pi \times 2.1$ GHz and the factor of $2/3$ is due to the coherent dark state that occurs in this transition. While being a much smaller contribution to the detection error due to being further off-resonance, the bright state pumping rate is included for completeness:

$$R_{\mathrm{b}} \approx \left(\frac{2}{3}\right)\left(\frac{\Gamma}{2}\right)\left(\frac{2\Omega^2}{\Gamma^2}\right)\left(\frac{\Gamma}{2(\Delta_{HFP} + \Delta_{HFS})}\right)^2 \tag{4.3}$$

Here, the $2/3$ is from the branching ratio of the $|F' = 1\rangle$ states decaying to the $|F = 1\rangle$ states, and $\Delta_{HFS} = 2\pi \times 12.6$ GHz is the hyper-fine splitting of the $^2\mathrm{S}_{1/2}$ manifold. With these scattering rates, it is possible to find the probability of detecting the ion's state when applying the detection laser, where the system has some detection efficiency ε_{sys} and background scattering rate R_{bg}. I will assume that a single count from the detector is the threshold for categorizing the ion to be in the $|\uparrow\rangle$ state. This is a good assumption as the aim is to use detection times that are an order of magnitude faster than the current four-rod system for which the detection threshold is at most two, and for which the detection setup is similar enough to suggest the background scattering should be comparable or better. To find the probability that we determine the state to be $|\uparrow\rangle$ given we've received $n \geq 1$ counts from the detector in a time t, we will instead use the complement (the probability of detecting $|\uparrow\rangle$ given no counts from our detector):

$$\begin{aligned} P_{t,|\uparrow\rangle}(n \geq 1) =& 1 - P_{t,|\uparrow\rangle}(n = 0) \\ =& 1 - \left(\frac{R_{\mathrm{d}}}{\varepsilon_{\mathrm{sys}} R_{\mathrm{opt}} + R_{\mathrm{d}}} e^{-R_{\mathrm{bg}} t}\left[1 - e^{-(\varepsilon_{\mathrm{sys}} R_{\mathrm{opt}} + R_{\mathrm{d}})t}\right] + e^{-R_{\mathrm{d}} t} e^{-((\varepsilon_{\mathrm{sys}} R_{\mathrm{opt}} + R_{\mathrm{bg}})t}\right) \end{aligned} \tag{4.4}$$

Similarly, the probability of determining the ion's state to be $|\downarrow\rangle$ given zero counts from the detector is:

$$P_{t,|\downarrow\rangle}(n = 0) = \frac{R_{\mathrm{b}}}{\varepsilon_{\mathrm{sys}} R_{\mathrm{opt}} - R_{\mathrm{b}}} e^{-R_{\mathrm{bg}} t}\left[e^{-R_{\mathrm{b}} t} - e^{-\varepsilon_{\mathrm{sys}} R_{\mathrm{opt}} t}\right] + e^{-R_{\mathrm{b}} t} e^{-R_{\mathrm{bg}} t} \tag{4.5}$$

A commonly used metric for determining how good the detection system is, and the types of simulations it is capable of is the average state-detection fidelity given by:

$$F = \frac{P_{t,|\uparrow\rangle}(n \geq 1) + P_{t,|\downarrow\rangle}(n = 0)}{2} \tag{4.6}$$

In the coming section I will explore the limitations and constraints that high state-detection fidelity puts on the system and how to overcome them with robust mechanical and optical engineering.

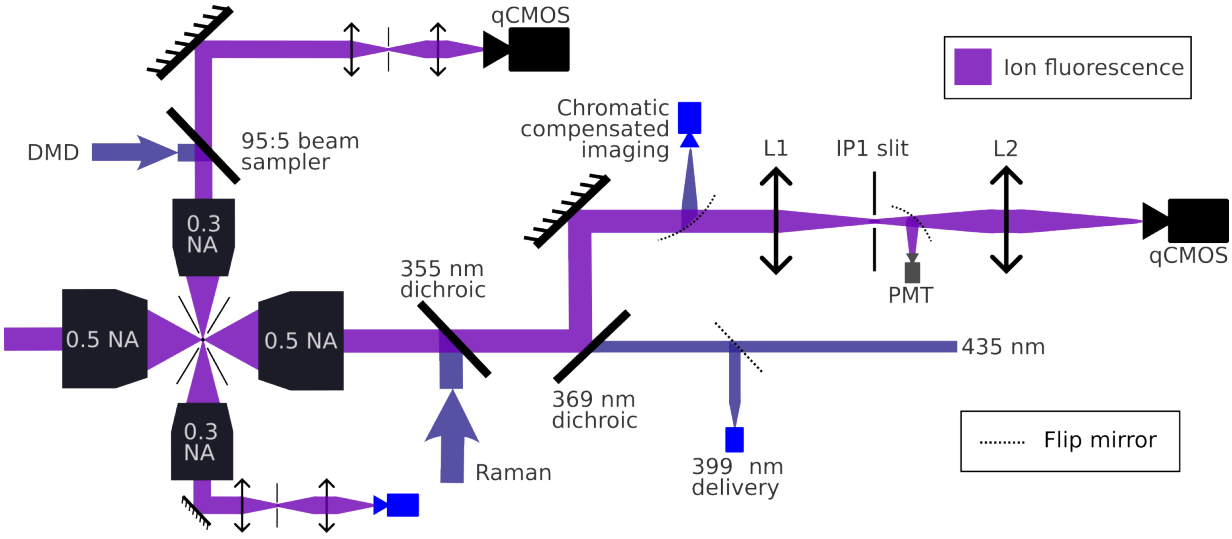


Figure 4.2: **Blade trap imaging layout.** Ion fluorescence is shown in purple while ion addressing from the DMD, 355 nm, and ionization beams are shown in blue. Two 0.5 NA custom made objectives from Photon Gear (P/N:18910) make up the symmetric two-sided imaging of the blade trap. A parabolic reflector will be mounted on a flip mirror to help align the 1 μm Raman beam to the ions. A flip mirror with a concave surface will be used to direct light on the a PMT detector for fast individual mid-circuit measurement. The top imaging system uses a 0.3 NA objective from Special Optics (P/N 1-293434) and will be used for experiments that require both mid-circuit measurement and global camera detection. The same objective will be used on the bottom to provide an unchanging reference to the ion while also making the alignment of the DMD to the ion easier.

4.3 Optical layout

While important, state detection is only one of many systems that requires optical access to the ion. Since space is limited, some of these systems will have to share resources and optical access in order for the quantum simulator to act as such. This section will discuss the design constraints put on the detection system.

Starting at the ion, the blade electrodes cut the NA of the system along the ion chain into two sections: the top/bottom with 0.44 NA each, and the right/left with 0.66 NA. Re-entrants are used to place the objectives as close to the ion as possible while still keeping them outside of the vacuum chamber. These re-entrants cut the NA of the sides down to about 0.6 while preserving the top and bottom. Two custom side objectives (left and right) from Photon Gear were ordered in collaboration with several other groups to reduce costs. These objectives cut the NA down slightly, to just over 0.5, for the detection light (369.5 nm). The top and bottom objectives, designed by Special Optics, also cut the NA down slightly to 0.3.

The primary imaging system will utilize the two side objectives in a mirrored setup, one side of which can be seen in Figure 4.2. These objectives will be shared with two co-propagating 355 nm beams used for the two qubit operations. To combine the 355 nm beam with the imaging system, a 355 nm dichroic is used. This also has the effect of filtering out the 355 nm light on the way to the detectors. Trapping ions requires 399 nm light to be focused at the trap center for exciting the first ionization transition, which provides the isotope selectivity. Future plans may also require the use of 435 nm light, which could be used for sympathetic cooling during simulations. Placing a 369 nm dichroic offers the ability to easily combine these beams into the imaging path. This dichroic, along with a mirror, will be placed on 2" Polaris mounts. This will give full control over the beam which will be useful when aligning the system. To focus the beam down to an intermediate image plane (IP1), the lens system L1 was used. Placing an adjustable xy-slit at IP1 reduces background scattering while still retaining all the light from the ions. The lens system L2 will be used to relay the image at IP1 to the camera and to reduce the total magnification of the system to 5. A magnification of 5 is needed to ensure that each ion is still confined to one pixel ($\sim$ 80% enclosed energy) of the Hamamatsu qCMOS camera (4.6 μm $\times$ 4.6 μm, C15550-20UP) while also separating neighbouring ions by roughly three dark pixels in order to increase detection fidelity.

For the fast detection times required for mid-circuit measurement, it will be necessary to use a PMT (Hamamatsu H10682-210). In the 4-rod system, a flip mirror is placed just before the qCMOS camera to focus the light down on a PMT. Initial back-of-the-envelope calculations suggested that the difference between being able to achieve 99% and 99.9% detection fidelity was the placement of only a few FS lenses. The effects of additional lenses turned out not to be as limiting as first thought. This was primarily due to inaccurate transmission efficiency values that were used in the initial calculation. Nevertheless, at some point this will become the limiting factor in reaching high detection fidelity during mid-circuit measurement, so reducing the number of elements before the PMT will help increase the robustness of the imaging system. Rather than building a separate imaging

system for the PMT, a flip mirror is placed just after the slits at IP1 to direct the light onto the PMT. This has the added advantage of sharing the slit at IP1 which can be optimized with the camera by centering the ion chain while focusing on the horizontal slit. As the light is diverging at this point, the original design would have required a lens to confine the light of each ion in the chain onto the 8 mm sensor of the PMT. Instead, a concave mirror was used. This has the same effect while preventing additional losses due to UV transmission through the medium. As the PMT is one large sensor, the additional optical aberrations introduced here are of no concern. To help reduce the amount of time that the detection beam is shining on the ions, the plan is to deploy photon time tagging with our PMTs. This concludes the primary imaging path for the blade trap system. However, there are a few other secondary imaging systems that I will briefly cover.

To give more control of two qubit interactions, the Raman beams will be focused down to a 1 μm beam waist to individually address each ion while reducing the intensity cross talk to below 10^{-4}. With the difficulties of aligning the 3 μm beam waist of the four-rod system still fresh in our minds, we require an intelligent way of aligning these beams onto the ions. With the Raman laser shining near the ions there will, no doubt, be leaked light through the 355 nm dichroic onto the imaging path. Using this as an advantage, a flip mirror will be placed to direct this light, along with the light from a single trapped ion, onto a chromatic compensated imaging system. This will allow the 355 nm beam to be aligned close enough to the ion that it should be possible to drive Raman transitions which can be used for fine adjustment. If a regular flip mirror were to be placed in this path, there would then be a need to design a lens system that can compensate for the focal length difference that the 369 nm and 355 nm have when traveling through different materials.[3] A much simpler approach is to place a parabolic reflector on this flip mirror in order to both redirect and focus both beams to the camera. While this may introduce some additional aberrations, it should be good enough to get a Raman signature on the ions.

The top objective will be used to bring the aberration corrected, individual addressing DMD system to the ions. During a quantum simulation, it is often helpful, if not required, to measure each ion's state independently at the end of each experiment. This state detection is often done with a high quality, low noise camera (qCMOS camera for instance). If these simulations also require mid-circuit measurement, then the primary imaging system will be set up for PMT detection, and switching the beam path is not a feasible approach to performing the final camera detection. For this reason, there will be a secondary imaging system using the top objective and a similar design to the primary side imaging with lenses to focus down to IP1, a slit to cut down on the background scattering, and imaging of IP1 to the camera in order to achieve the 5 times magnification. By using a 95 : 5

[3] As is the case in our custom 0.5 NA objective.

beam sampler, most of the light from the ions detection process will be let through to the qCMOS camera while still allowing for the ability to address the ions with the DMD system. Similarly to aligning the 355 nm beam, the beam waist size from the DMD will be on the 1 μm scale. To help align this beam to the ions, the bottom objective will be used to directly image the ions and DMD beam onto the sensor of a camera. This method of alignment has been implemented in the 4-rod trap and has proven to be a valuable tool when adjustments are done to the system. With the constrains of the blade trap system understood, I will proceed to explain the process of designing a robust imaging system that is capable of mid-circuit measurement.

4.4 Design requirements for mid-circuit measurement

In this section I will explore the different requirements that the imaging system must meet in order to perform robust mid-circuit measurements during quantum experiments.

4.4.1 System efficiencies

When designing a robust imaging system, the constraints on the type and number of optical elements used must be considered. This is sometimes due to space constraints. Here, however, we are concerned primarily with the transmission efficiency of light through the optics. Effects such as photon absorption enter our fidelity measurement through the system detection efficiency parameter ε_{sys}. We break this total system detection efficiency further to give:

$$\varepsilon_{sys} = \varepsilon_{NA}\varepsilon_{objective}\varepsilon_{detector}\varepsilon_{filter}\varepsilon_{lens} \tag{4.7}$$

ε_{NA} is the amount of solid angle our imaging system is collecting and is found to be:

$$\varepsilon_{NA} = \frac{1-\sqrt{1-NA^2}}{2} \tag{4.8}$$

For one side of our 0.5 NA imaging system this evaluates to $\varepsilon_{NA} \approx 0.058$. The two sided imaging of the blade trap will need to be used when performing high fidelity mid-circuit measurement so we double this number for the following simulations. Our custom objective is made of lenses and thus will have some transition efficiency $\varepsilon_{objective}$. Taking the conservative value for 355 nm light from the manufactures data sheet, this gives $\varepsilon_{objective} = 0.9$. Not every photon that hit's our detector will register a count. The detector efficiency was calculated from the sensitivity of the detector at our detection frequency and found

to be $\varepsilon_{detector} = 0.32$. As mentioned in Section 4.3, our imaging system shares a path with the Raman beam. The 355 nm dichroic and 355 nm filter needed on the PMT have transmission values for 369 nm that are easily found on the data sheet. These combine to give $\varepsilon_{filter} = 0.95^2 \approx 0.9$. ε_{lens} accounts for the transmission efficiency of the Anti-Reflective (AR) coated FS lenses and is 98.6% for a piece of FS 3 mm thick (numbers from Edmund Optics). This number includes the slight amount of reflections seen at the surface which is quoted to be less than 0.5% so we expect the transmission efficiency to be approximately 99% for every 3 mm of FS material. On average, each lens in 5 mm so if we let n be the number of lenses in our system we have:

$$\varepsilon_{lens} = (0.995^n)\left(0.99^{\frac{5n}{3}}\right) \tag{4.9}$$

4.4.2 Attenuation of a classical beam

The robustness of our state detection system relies on the detection of only a few photons during an experiment. Since imaging shares an objective with our classical Raman beam, we must ensure that our 355 light is not leaking onto the detector. This would cause false detection events which, if numerous enough, would lead to reduced detection fidelity. To combat this issue we can install filters that block 355 nm light, while letting 369 nm light through. These filters, however, are not 100% transmissive at 369 nm and so adding as few as possible will allow us to reduce our detection times for mic-circuit measurement. To get an idea of how much we must reduce our 355 nm light, we can start by calculating the number of 355 nm photons per second our system will have while performing quantum simulations. The current design for the Raman system is to have the ability to individually address 32 ions with at most 1 mW of power each. For simplicity lets round this to a 50 mW Raman beam. With this intensity and the energy of a single 355 nm photon (hc/λ), we find the rate (photons per second) of our Raman system to be 9×10^{16} Hz. We want to reduce this value so it is on the same scale as the scattering rate of our ion. However, these two systems differ somewhat. Our Raman beam will be focused onto the ions from the opposite side objective meaning that all the photons entering the system will be collected by the imaging objective. This is in contrast to the ion which scatters photons in all directions, only some of which are collected by the imaging objective. In the next section we will look closer at this collection efficiency but for now we will take it to be 5%. The dichroic used to bring the Raman beam to the ions will also have a slight effect of the detection scattering rate, with a transmission efficiency of 95% at 369 nm. Assuming we'll require at least one filter at the PMT to avoid it from saturating while the ion is being addressed with a Raman beam, we'll add an additional 355 nm RazorEdge filter that too has a transmission

efficiency of 95% at 369 nm. The rest of the system, lenses and mirror are going to have similar effects on 355 and 369 nm light so their contributions do not need to be accounted for.

Taking into account these restrictions (system efficiencies) on the ions scattering rate and using equation 4.1, gives us a detection rate of approximately 5×10^5 Hz (using a saturation intensity of $s_0 = 1$ and on resonant laser detuning $\Delta = 0$). Lets assume we are aiming for a (bright state) detection fidelity of .999 or, more appropriately, an infidelity of $1 - .999 = 0.001$. To insure our Raman beam does not have a meaning effect on the fidelity, lets aim for being below 1% of this infidelity. This means we want our Raman rate during measurement to be 1% of $5 \times 10^5 \times 0.001$ or on the order of 5 Hz. To help manage these large numbers we will convert this into a decibel scale. For us to reduce the Raman rate to a few Hertz, we require $\log_{10}\left(\frac{9\times10^{16}}{5}\right) \approx 162$ dB of attenuation. During the detection process we will not be addressing the ions with the 355 nm light meaning our AOM's will be off (no RF power sent to them). In a single pass configuration, we measure our Raman AOM's to have a first order attenuation of greater than $\log_{10}\left(\frac{10\ \text{mW}}{3\ \mu\text{W}}\right) \approx 35$ dB. Since our Raman setup will have these in a double pass configuration, that's approximately 70 dB of attenuation. If we assume our Acousto-Optic Deflector (AOD) will have similar level of attenuation, we then have a total of 100 dB of suppression before any filters or dichroic. Adding a single 369 nm RazorEdge long pass filter from Semrock will provide an additional attenuation of 60 dB (OD6) at 355 nm while being 95% transmissive at the detection frequency. With the effects of the dichroic, we should be able to sufficiently suppress the 355 nm light while performing state detection.

We have confirmed that the detection fidelity will be robust against leaked light from the Raman system. However, there is one other unknown factor in this setup. While addressing the ions with 355 nm light, the PMT may become saturated due to the increased number of photons hitting it. If the PMT does not relax to near its background counts quickly enough when starting the detection process, the type of simulations we can run may be limited. To get a rough scale of the problem, we now want to reduce the Raman beam, while shining on the ions, to a rate comparable to that of the scattering rate of the ion. This means we require $\log_{10}\left(\frac{9\times10^{16}}{1\times10^{7}}\right) \approx 90$ dB of attenuation. As stated above, the long pass filter brings this down by 60 dB. The 355 nm dichroic will add an additional 20 dB of attenuation. Depending on how the PMT relaxes to normal background counts when seeing this extra light from our Raman beam, we may need to add an additional filter to counteract this. Once the system is set up we will be able to get experimental data to confirm this and compare how the detection fidelity is affected by additional filters.

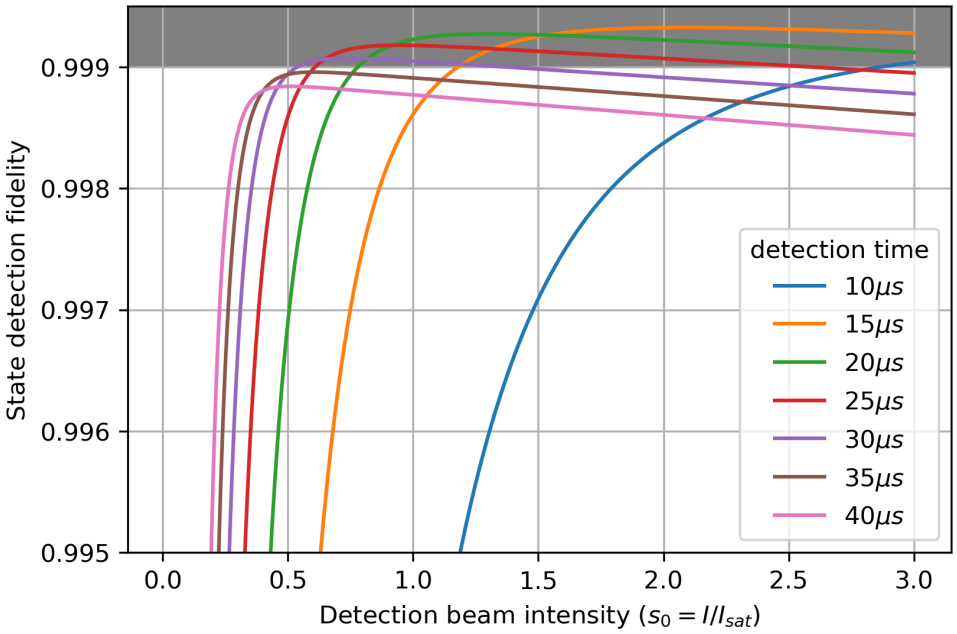


Figure 4.3: **State detection fidelity vs detection beam intensity.** Above is a plot of state detection fidelity vs detection beam intensity (I/I_{sat}) for different detection times. The grey region represents our target state detection fidelity of 99.9%. Calculations include system efficiencies and a background scattering rate of 50Hz, the limit coming from the PMT's dark count as quoted from the data sheet.

4.4.3 Reaching high state detection fidelity

As discussed in Section 4.1, to perform high fidelity mid-circuit measurements and unlock the full potential of our system, we require process times on the order of 11 μs. Recall that this means the detection times should be somewhere between 10 and 40 μs to reach high preservation fidelity during mid-circuit measurement. As we can see in Figure 4.3, this is not as simple as picking the shortest time if we are aiming for a state detection fidelity of say 99.9%. In these simulations we have taken into account the system efficiencies stated above with two lenses and a background scattering rate that is typical of the PMT dark count (50 Hz). For shorter detection times (10 μs), we require a much higher intensity detection beam to achieve the desired detection fidelity. This increase in intensity (beyond $I/I_{sat} = 1.25$) will increase the cross-talk that neighbouring ion see and thus reduce the preservation fidelity. Detection times of 40 μs require less optical intensity, but they reduce preservation

fidelity due to the increase in process times. A detection time of 20 to 25 μs seems to be the sweet spot between short process times and lower beam intensities. The truly optimal detection time will be heavily dependent on the type of quantum simulation we want to perform. Some experiments will require that the state of the system be preserved to very high fidelity and so a sacrifice must be made in the knowledge of the measured qubits state. Other experiments may be more robust and thus allow for achievement of the high state detection fidelity seen above (fig. 4.3). As we will see, there are numerous additional factors that impact the fidelity of state detection. Therefore, conducting a complete analysis of the relationship between detection and preservation fidelity will happen once the system is operational and there is an experimentally measured detection fidelity.

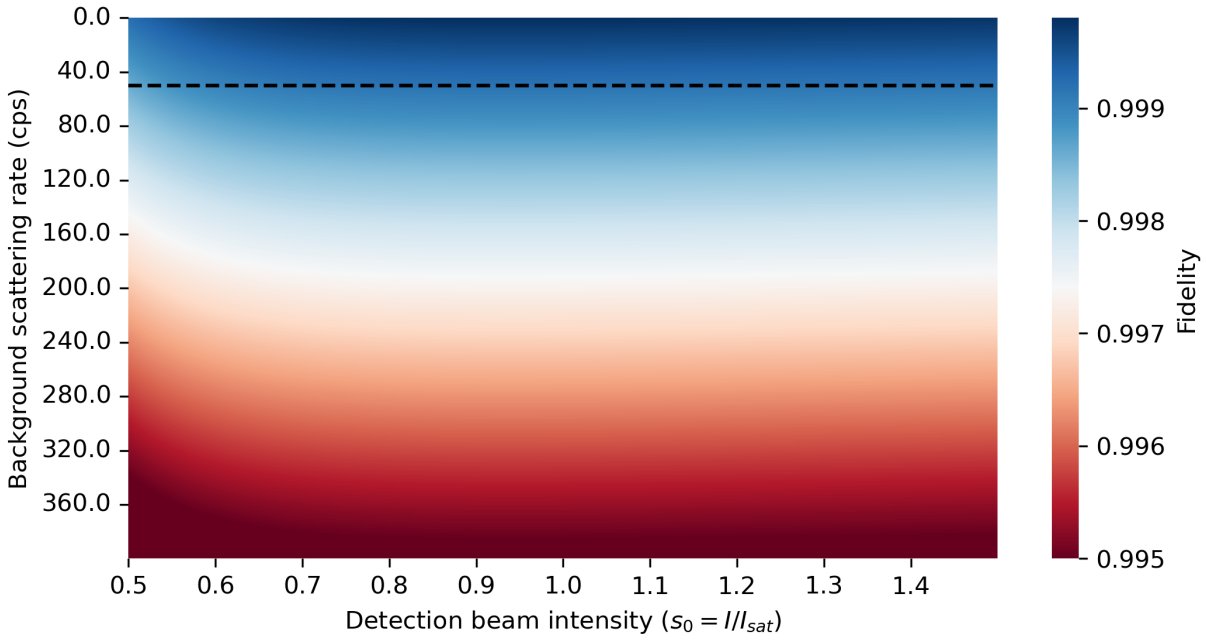


Figure 4.4: **Background scattering rate.** The above colour map shows state detection fidelity vs background scattering rate and detection light intensity. Simulations include the effects from system efficiencies with a detection time of 25 μs. The dashed line indicates the typical dark count for the PMT (50 Hz).

Now that we have an understanding of how detection time can effect fidelity we can look at the other limitations our system can encounter. Next to detection time, the back ground scattering rate becomes the limiting factor in our state detection fidelity. Figure 4.4 shows ion detection fidelity as a function of background scattering rate measured in

counts per second (cps) and detection beam intensity (I/I_{sat}). This simulation considers a detection time of 25 μs and takes into account our system efficiencies with two lenses. The bashed line in the plot shows the typical dark count rate of the PMT in our system. We can see from this figure that if we do not carefully cut down on the additional background scattering from say our detection beam, we will be limited to detection fidelity values below 99.9%. It should also be clear that even with no excess background scattering, our detector will be what limits us from achieving the fourth 9 in our detection fidelity.[4] This is were detectors such as the SNSPD would have to be used to reach the near zero background counts. By cooling the PMT, we may be able to push this line a meaningful amount, although we may encounter issues with condensation if surfaces are too cold.

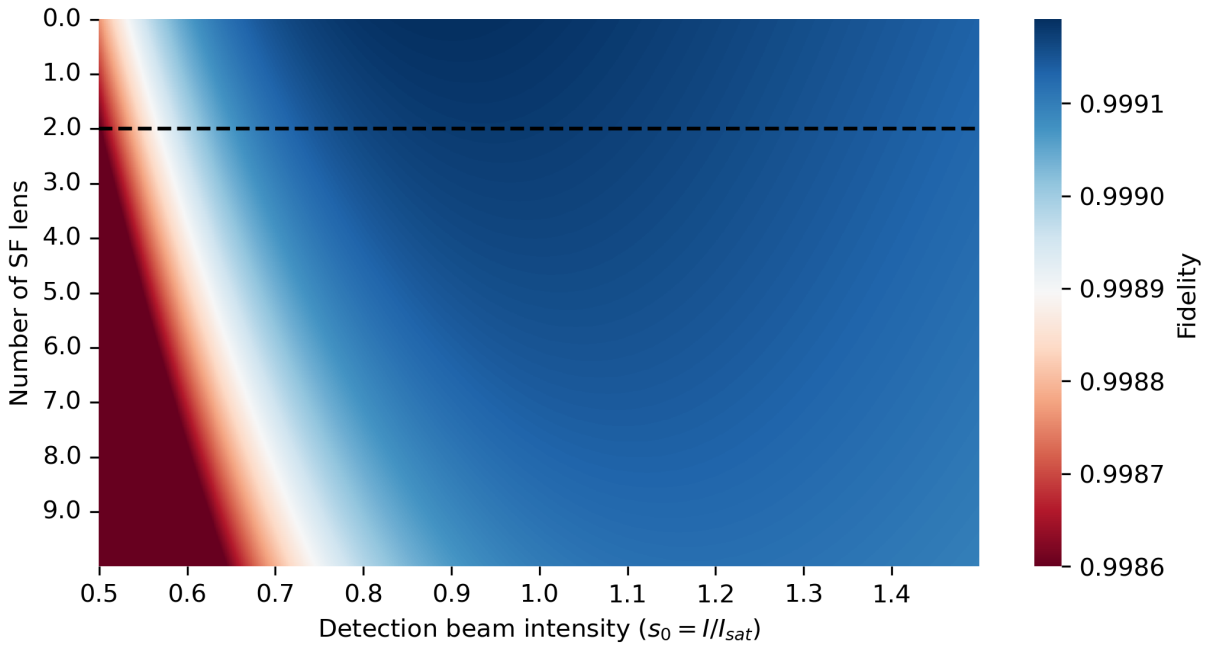


Figure 4.5: **Effect of lenses on state detection fidelity.** The above colour map shows state detection fidelity vs number of Fused Silica lenses and detection light intensity. Simulations include the effects from system efficiencies with a detection time of 25μs. The dashed line indicates the number of lenses in our current mid-circuit measurement system (2).

As discussed in Section 4.4.1, initial calculations suggested that adding additional lenses

[4]Initial tests of the PMT dark count were able to achieve a rate as low as 5 cps by carefully shielding of the system, a promising result.

would greatly reduce the detection fidelity. This was due to using transmission efficiencies for uncoated FS which did not take into account the effects of reflection at the surface. Once the transmission efficiency numbers for AR coated lenses were found these investigations were updated. Figure 4.5 shows how the number of lenses in the system prior to the detector effect the state detection fidelity. Again detection times here are 25 μs and other system efficiencies have been accounted for. The dashed line shows the number of lenses we plan to have in our system before the PMT detector. As we see, increasing the number of lenses does lead to a reduction of fidelity (as expected), although this effect is only in the fourth decimal of fidelity. As trapped ion systems try to push the boundary and achieve four nines of state detection fidelity the number of lenses may become a real concern. Future systems may have to sacrifice an increase in optical aberrations, in order to reduce the number of lenses to reach high enough fidelity. The error in the initial calculation that forced us to rethink the placement of the PMT may have been a blessing in disguise. As we will see in the following section, the space constraints near the camera are very limited so repositioning the PMT has the benefit of allowing more room for the alignment of the camera to the imaging beam focus. As we've learnt on our four-rod system, the quality of this alignment has a noticeable effect on the detection fidelity when using the qCMOS. When focusing down to IP1 we have increased our magnification to 11 which means the beam diverges from the slit far slower than it converges to the camera where the magnification is 5. This means the beam size stays smaller for a longer distance making it easier to bend and align to the sensor of the PMT. Now that we have an understanding of how to reach high fidelity mid-circuit measurement and the constraints that has put on our system we can start designing a robust imaging setup for our blade trap.

4.5 Blending mechanical and optical engineering

In this section we will explore how mechanical and optical engineering have been used to develop a robust state detection system for our blade trap.

4.5.1 High NA mechanical engineering

Designing a robust imaging system starts at the objective and the mounting on which it stands. If large instabilities are able to enter the system here, optical engineering may not be able to account for them. To quantify this number, we want our system to stay aligned to the ions within a few microns while people are working on neighbouring systems. If we cannot achieve this, valuable resources will be exhausted realigning the system every time

a screw is tightened. Our initial designs for the objective mounting used Polaris mounts fixed to a 3-axis translation stage which was mounted on the surrounding table. A plate with adjustable prongs (similar to that in fig. 4.6) was fixed to the vacuum chamber. Our plan was to first align the objective to the ions, tighten and glue the prongs against the objective and remove the aligning apparatus. While testing the system stability by imaging a fiber tip onto a camera, we found our system to be stable to within several microns (± 5 μm) with just the aligning stage and mirror (without clamping or gluing the prongs). A problem then arose when removing the aligning stage after clamping and gluing the prongs. When weight was transferred to the mounting plate from the initial aligning stage, a large shift in the beam would occur. With our aligning stage no longer attached to the objective, we would have no way of bringing back the systems alignment to an ion. We then went back to the drawing board to redesign the mounting to keep the aligning apparatus in place.

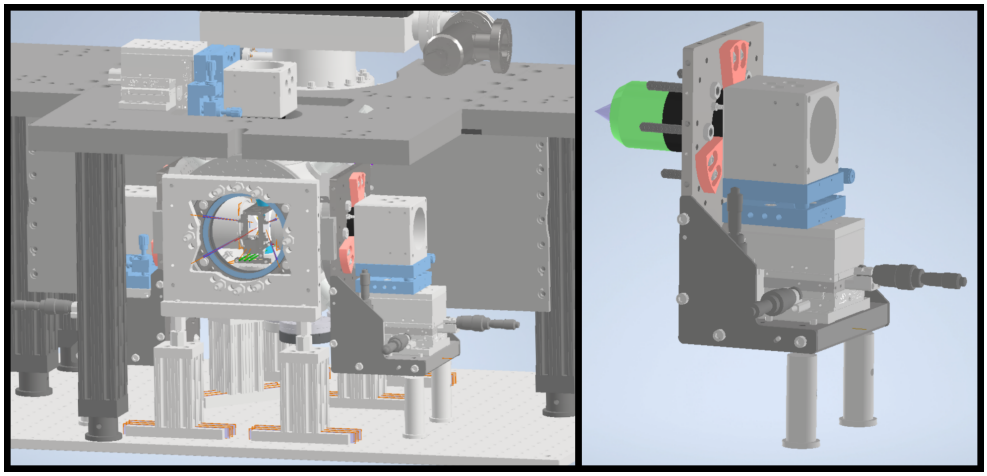


Figure 4.6: **CAD design for the blade trap imaging system.** The left shows the full assembly with vacuum chamber and 3$^{\text{rd}}$ floor blase plates used to mount the DMD and top imaging systems. The right shows a close up of the side objective mounting.

Figure 4.6 shows the current design for the blade trap objective mounting. The left shows the full assembly with vacuum chamber, top and side objective mounting, along with (what we're calling) the 3$^{\text{rd}}$ base plate that will be used to mount the DMD and top imaging. Similar plates will be used for the Raman and side imaging but have been hidden to increase viability around the chamber. The side objective mounting can be seen on the left of Figure 4.6. Similar to our previous design a stainless steel plate is mounted to the vacuum chamber with prongs that can be tightened on the objective to increase the

stability of the system. This side plate supports a base plate that will allow us to mount a 3-axis Newport translation stage as well as a two axis tilt stage. We will incorporate the motorized control from Section 3.3.2 on these stages to give us the fine alignment needed while keeping unstable hands away from the system. The objective mounting cube sits on top of the 2-axis tilt stage and, as the name suggest, mounts the objective to the system. The approximately 400 g objective is recessed into the cube and screws into treads to ensure adequate support and increased stability. Two fine tread set screws provide point contact on Thorlabs pedestals that sit under the base plate. This will be used to reduce the weight hanging off the vacuum chamber while not over constraining the system. Using spacers to set the distance of the mounting plate to the chamber will give a reference to the ion. This also allows us to use the prongs as a safety measure and prevent the objective from hitting the glass window of the re-entrant. A similar design is followed for the top objective mounting with the 2-axis tilt stage mounting on the front face of the 3-axis translation stage. Now that our objective has a stable reference to the ion we can start designing the optical system used to image the ion on the camera and PMT

4.5.2 The art of optical engineering

Before diving into the optical design and performance of the blade trap system I'd like to take some time to provide a helpful guide to anyone trying to build an imaging system for the first time. Many will say optical engineering is an art that requires intuition to be efficient in this process, I'm hoping this quick guide will help build some of that intuition. For this guide I'm assuming the reader is using a software such as Zemax to perform simulations and optimizations on the system. Before we get started I'm assuming you have some requirements of your imaging system that have been determined such as field of view, magnification and spot size to name a few. There are a few helpful tools I'd suggest using to get a sense of your systems performance. The spot diagram shows the distributions of the simulated rays at the image plan of choice, giving a good visual indication of the spot size. The enclosed energy diagram compares your system to a diffraction limited beam. This is often more important than the aberrations seen on the spot diagram when considering single pixel imaging, since it gives information on the percentage of light in a single pixel. When aberrations are of a concern, the optical path difference can be used to help quantify this and put a scale to the aberrations at the image in terms of the wavelength of light being simulated. The Seidel coefficients provide a more in depth analysis of the aberrations and show exactly which element is producing which aberration. If you are concerned with a field of view you may want to use the footprint diagram to visualize all fields you've simulated for. The merit function editor is a tool used when optimizing your

system. If there is some constraint your system must have you can almost guaranty there is a merit function that will help optimize your system for it. Merit functions can set a magnification for your system and make sure your optical elements are physically possible and reasonable. Assuming your trying to use off the shelf lenses, I found it helpful to create an excel sheet of all available lenses in the size, material and coating you want to use for your system. Make sure to list the part number, focal length, radius of curvature and if budget is a concern the price. This will save you from having to navigate websites designed in the mid 2000's while picking optical elements to use in the system.

Once you set up your initial conditions (type of source/image, NA and wavelength to name a few) perhaps the largest hurtle when designing an optical system is find out where to start? Using an existing setup will allow you to get your feet wet. These can be found in online examples or from previous group members optical systems. It is more likely than not that these initial trials will be abandoned but they serve as a starting position and help to gain some intuition on how real world optics behave. If you are going to abandon a project I suggest starting a new file rather than over writing the old one. While a system may not seem to have any use right now, as you progress there may be aspects of a system that you may want to replicate in the final project. Having an achieve that is easily accessible will save you a lot of trial and error as you try to recreate your previous work. Once you've got comfortable with the controls, placing and optimizing lens spacing I found it helpful to start new with a single lens. Then optimizing for the two outer curvatures and thickness of the lens, assuming you've set boundaries to make something physical, will likely lead to a system with very good performance. Now try to replicate this design using off the shelf components, starting with lenses that are of similar curvature to the ideal lens you've created. Optimize the distance between lenses (and to the focus) and run the analysis mentioned above to check the systems performance. It's probably not great, but we'll get there. Try a few different combinations of lenses and keep optimizing for the curvature for the lenses (but not the thickness), one surface at a time. At this point you should be trying as many different systems as your bandwidth can handle. It's this trial and error that builds intuition but to help give you a heads start I will list a few helpful tips. This is not an exhaustive list nor is it applicable in all cases but should help for someone starting out.

- At the end of the day, your trying to bend the light rays to some point. It is generally better to bend light gently, rather than aggressively. This helps to reduce aberrations and gives you a higher chance of correcting for the aberrations you do introduce.
- If possible, start with designing a low NA system. As the old saying goes; more NA more problems.

- Best form lenses are great for bending light a lot while keeping aberrations low. Incorporating them as part of the system can be great but their variety is usually limited.
- Two lenses of a longer focal length are often better than a single one with a short focal length, although this is not a law of physics and the opposite can be true in some scenarios.
- Similar to the last point, having light travel through less glass will lead to less optical aberrations, so thinner lenses should often be the first choise.
- When correcting for spherical aberrations, you often balance the positive curvature of the convex lenses with the negative curvature of a single (or possibly 2) concave lens. By reversing the orientation of the concave lens to the non-optimal direction (flat surface towards the focus) you will introduce a large amount of negative spherical aberrations that can be used to balance the positive spherical aberrations a from many convex lenses. That is to say, don't be afraid if one element introduces a large amount of aberrations if the rest of the system corrects for them. [5]
- If you have two plano-convex lenses in your system try replacing one with a positive-meniscus lens. You may find that you can focus tighter while reducing aberrations.
- Similarly, try replacing the a plano-concave lens with a negative-meniscus, again in the non-optimal direction.
- Typically plano-convex lenses perform much better that bi-convex lenses but for some systems bi-convex lenses are exactly what is needed.
- Reverse lenses (and even the system) often, it's just one click of the bottom and could lead to some promising results.

I'll leave the reader with one last piece of advice: as you start to build the intuition you will realize that the system is never fully optimized, you simply lose patience or run out of time, it's normal.

With an understanding of how to design optical systems, we will now look at the performance of the blade trap imaging starting off with a bit of house cleaning. The Zemax files for the side objective where sent in the form of a black-box, which is meant to accurately simulate the objective performance while not giving away the internal design.

[5] or perhaps you can think of this single lens correcting for the rest of the system.

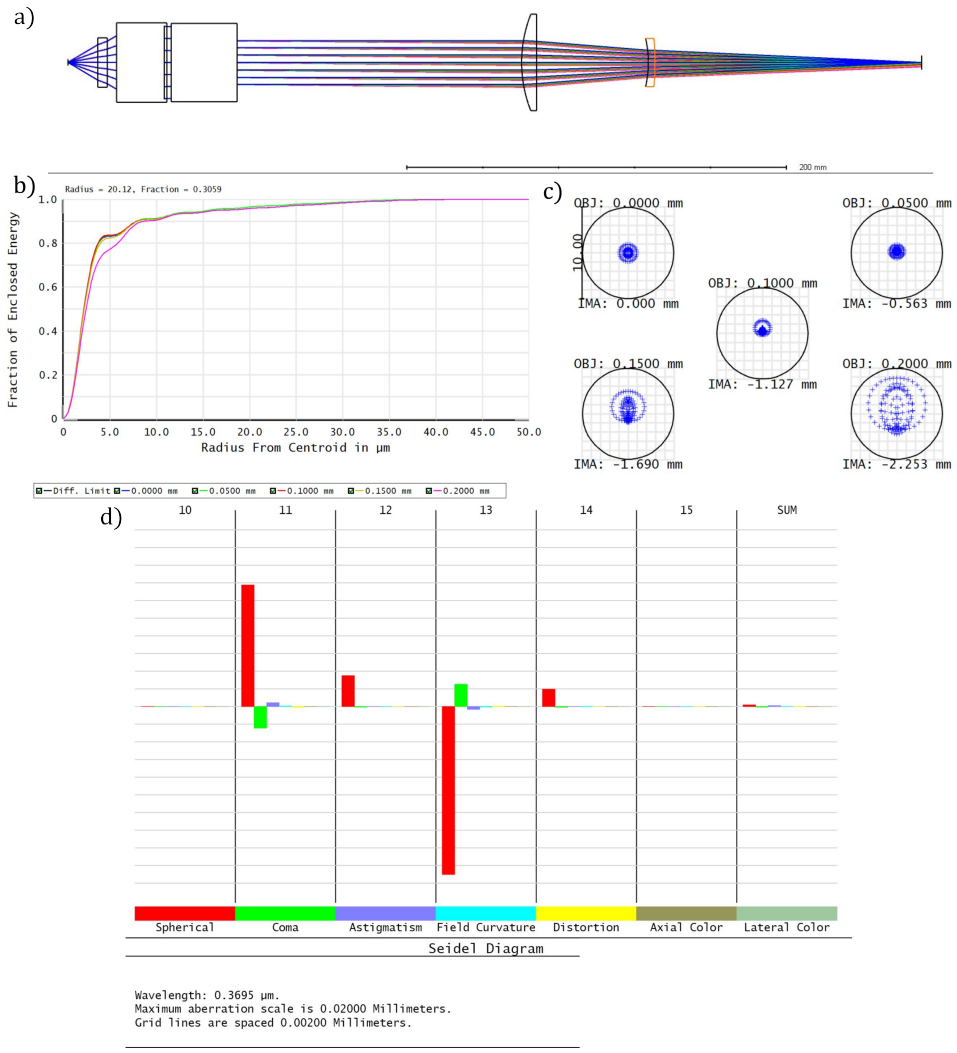


Figure 4.7: **Doublet simulations.** The above shows the Zemax simulation for the doublet in the blade trap imaging system that focuses the beam down to IP1. a) is a optical schematic showing the custom made 0.5 NA objective from Photon Gear (represented as a black box optics files) and doublet. b) shows the fractional enclosed energy as a function of radial distance. c) shows the spot diagram at IP1 for fields from center to 200 μm in steps of 50 μm. The Seidel diagram (d) shows the optical aberrations introduced at each lens surface and summed at IP1.

The files include the re-entrant window and the distance between it and the focus was checked to match the location of our ion in the vacuum system. Figure 4.7a shows a two lens design (often called a doublet) that focuses the light down to IP1 with a magnification of 11. The doublet is comprised of a 2" plano-convex lens with a focal length of 150 mm and a 200 mm focal length, 1" negative meniscus lens. The beam size out of the objective has a diameter of roughly 18 mm so the 1" lens is placed where the beam has decreased in size so that there is no clipping of light at the edge of the lens. A custom spacer made out of aluminum will reference these lenses together in a 2" lens tube. The enclosed energy can be seen in Figure 4.7b. The different colour lines show the enclosed energy for fields from 0 to +200 μm from center (in increments of 50 μm) which is slightly larger than the extent of large ion chain. There is a black line that shows the ideal diffraction limited enclosed energy and is hidden under the field lines of 100 μm and closer. In Figure 4.7c we can see the spot size all the way up to 200 μm from center are confined within circle with a diameter of 7 μm. The Seidel diagram in Figure 4.7d shows while individual components have added large amounts of spherical and coma aberrations, they have been successfully suppressed at IP1. While the original constraint restricting this system to two lenses turned out not to be as limiting as first thought, it forced the design to evolve and incorporate the 1" negative meniscus lens which ended up giving really good performance, equal to or better than most three lens systems that were also simulated.

In Figure 4.8 we can see the Zemax simulation for the full blade trap imaging system including the doublet and objective from above. The additional optics serve to relay the image at IP1 to the camera while setting the magnification for the system to 5. To do this I have used the following 2" lenses; a 150 mm focal length plano-concave lens, two 200 mm focal length positive meniscus lenses, and a bi-convex lens with a focal length of 150 mm. If we do not focus the light from an ion down to a single camera pixel, our camera state detection fidelity would be greatly reduced. From the enclosed energy, we can see that 80% or more of the lights energy is confined to the radius of a single pixel of the qCMOS camera (4.6 μm $\times$ 4.6 μm) up until 150 μm from center. From the spot diagram we can see that our beam is spread out more than at the intermediate image plan. This means that our alignment to the center of the ion chain will be very important for maximizing the detection fidelity of the camera. The Seidel diagram shows a slight positive spherical aberration in the image plane (last column). The main contributes to this are the two surfaces of the bi-convex lens so perhaps this lens could be further optimized. As this is a high NA system, once we've aligned our system to the ion we may find that we have an excess of aberrations that aren't easily taken away from adjusting the mirrors or objective. These can be due to slight misalignment's of the lenses due to imperfect spacers or tilts added to the beam that are uncorrectable. One way to correct for these aberrations is to

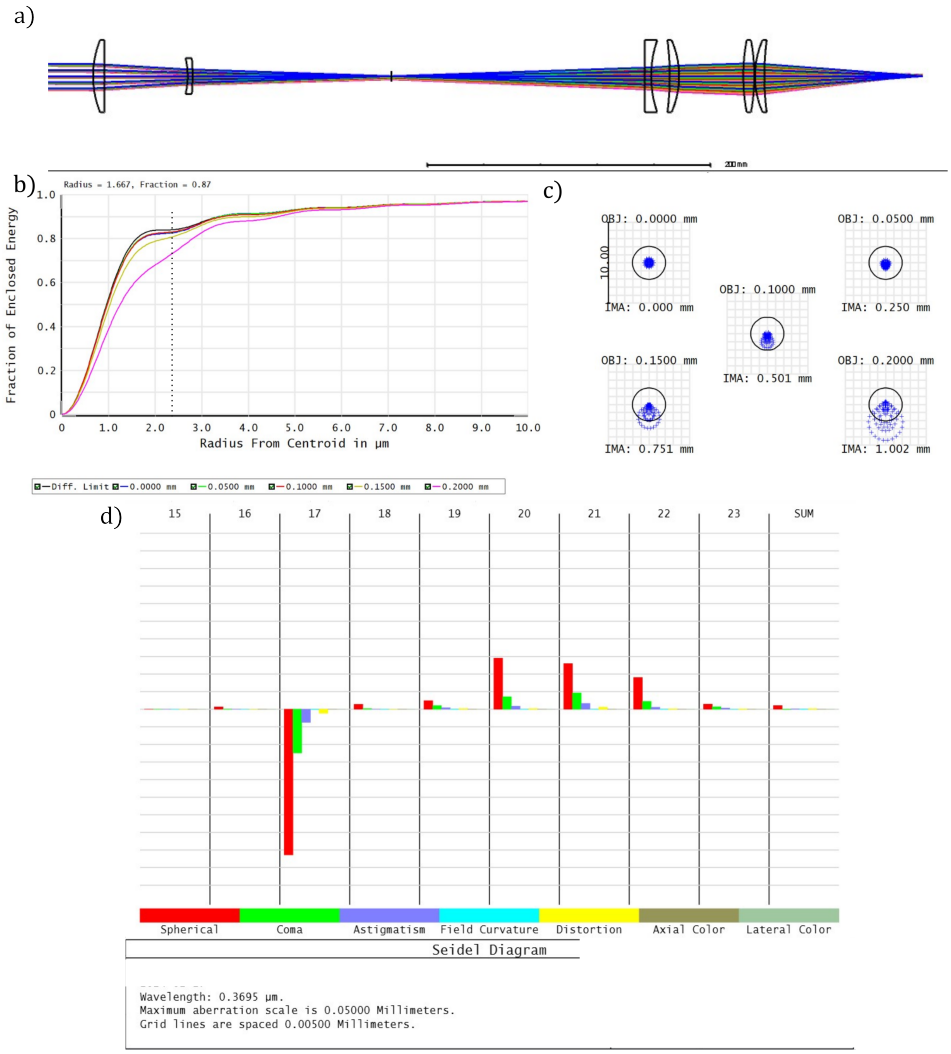


Figure 4.8: **Doublet simulations.** The above shows the Zemax simulation for the full blade trap imaging system to the qCMOS camera. a) is a optical schematic showing the doublet and relay imaging system. b) shows the fractional enclosed energy as a function of radial distance. The dashed line indicates the size of a single pixel on our camera's detector (4.6 μm $\times$ 4.6 μm). c) shows the spot diagram at the camera sensor for fields from center to 200 μm in steps of 50 μm. The Seidel diagram (d) shows the optical aberrations introduced at each lens surface of the relay system.

slightly adjust the position (both transnational and tilt) of one of the lenses depending on the aberrations we are seeing. By making small adjustments to each of the lenses in the system above, and considering the feasibility of performing these movements, it was determined that the 2" plano-concave mirror gave the best control while being easily access in the system. Once we align the system to the camera in a test setup we can determine whether or not the control is needed.

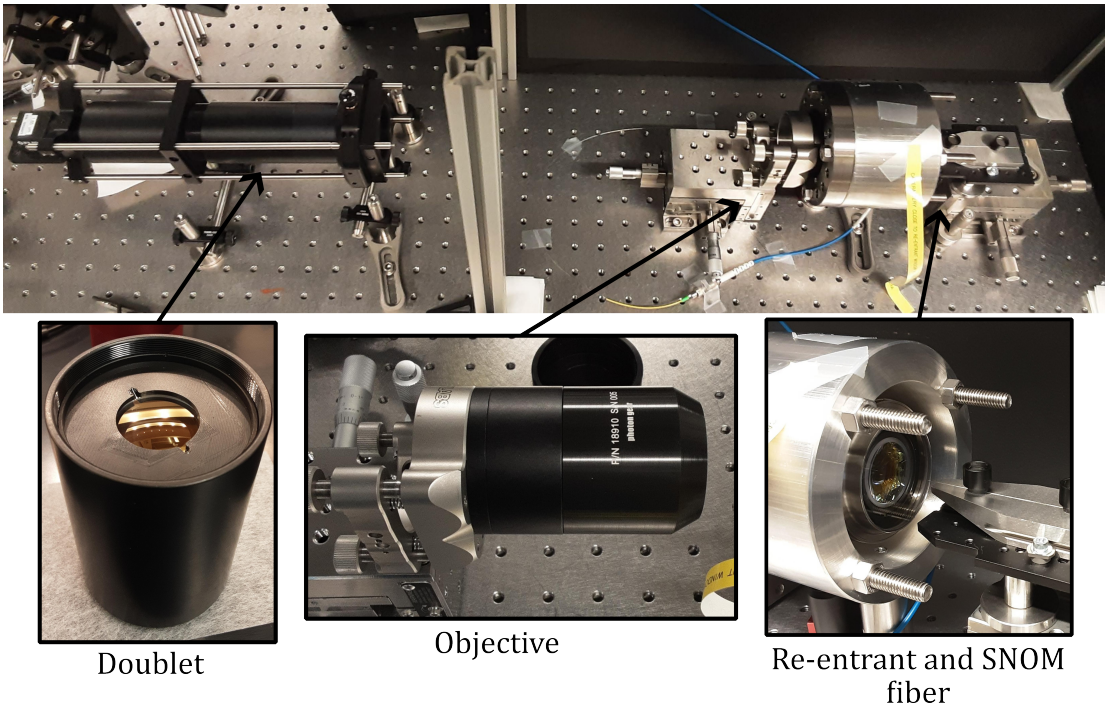


Figure 4.9: **Doublet test setup.** The above shows the setup used to test the performance of the doublet. An SNOM fiber with a 100 nm aperture was used to mimic the ion acting as a point source. The 0.5 NA objective was placed inside the re-entrant and aligned to the fiber. An FLIR camera with a square pixel size of 1.85 μm was used to image the fiber at IP1 after the doublet.

4.6 Doublet testing

Now that we have a design ready we need to start testing components to verify that we can achieve similar levels of performance compared to the simulations. To do this we use a

SNOM fiber with a aperture of 100 nm to mimic an ion. Since the fiber tip is smaller than the wavelength of our light (369 nm), it can be assumed to be a point source making it suitable to test our 0.5 NA imaging system. Figure 4.9 shows the test setup. An aluminum sleeve is used to rigidly mount the re-entrant and keep it protected from the sides while still giving access to the front surface. The SNOM fiber is fixed to a v-grove mount on a 3-axis translations stage and positioned roughly center on the re-entrant window and at the ion location. The 0.5 NA objective was mounted to a Polaris mirror mount which itself sits on a 3-axis stage. The front surface of the mirror mount acts as a stop to prevent the objective from hitting the glass surface of the re-entrant. Lens tubes were used as spacers to get this distance to 4 mm which is slightly larger than the 1 mm distance we've engineered into our actual objective mount. A 3D printed spacer was used to reference the 2" doublet to the 1" negative meniscus lens which was glued in place. An FLIR camera with a pixel size of 1.85 μm was used to image the beam.

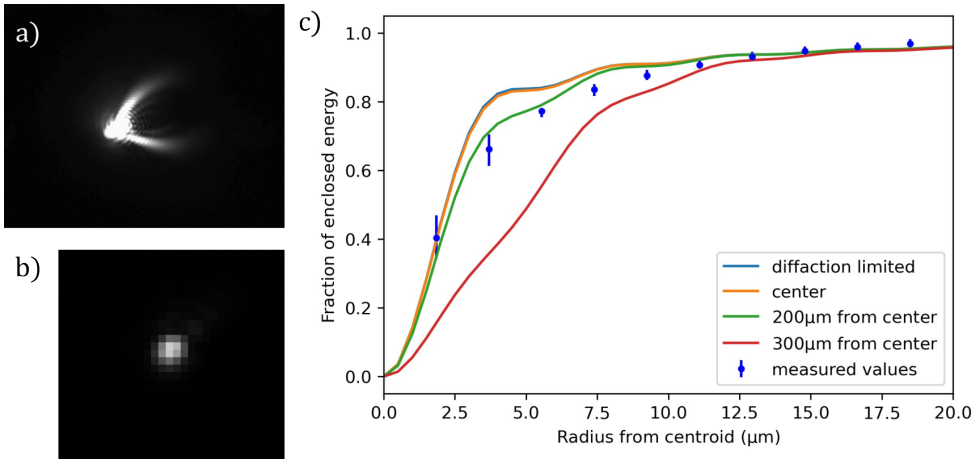


Figure 4.10: **Doublet testing measurements.** a) shows the initial beam focused after the doublet focused onto a FLIR camera while b) shows the final result after alignment was complete. c) shows the measured and simulated values for the enclosed energy. Multiple measurements where taken for different beam intensities and slight shifts in objective-fiber focus and were used to get the min-max error bars. The simulated data for the enclosed energy was taken from the Zemax simulations for the doublet.

Alignment of a high NA system poses many challenges. Taking a systematic approach can help reduce the time required to achieve performance with minimal aberration. When placing components like the re-entrant, care was taken to align it to the grid of the optics table so it could be used to help reduce the tilt of the objective with respect to the re-entrant

window. Using the grid and a height reference the beam could then be leveled across the length of the optics table. The same distance (approximately three meters) could also be used to collimate the beam out of the objective. Once the beam was collimated, the doublet was brought in and the camera was positioned at the focus. As the tilt of the objective changes so to does the focus so this step made easy work of re-collimating the beam (and thus focusing on the camera). In Figure 4.10 a) we can see the initial image of the beam, with a large amount of spherical and coma aberrations. Since the objective NA is much greater than the doublet, it is going to be the likely cause of most of the aberrations in the system (initially at least). By adjusting the tilt of the Polaris mirror holding the objective, and scanning both the position of the fiber and objective, we slowly start to reduce the aberrations. Throughout this process, the horizontal, vertical and tilt position of the doublet and camera system where adjusting to find the new optimal point. Figure 4.10 b) shows the final beam after aberrations were minimized. Some slight aberrations could be seem when decreasing the camera's Gamma setting to very low values (< 0.3). With the doublet imaging aligned, the power of the beam was reduced so that the beam was not saturating any pixels of the camera for a 10 μs exposure time, zero gain and Gamma set to 1. Several photos were saved at slightly different beam powers and the beam waist was calculated and found to be about 4.5 μm. The distance of the fiber and objective to the window was also adjusted slightly while keeping the beam in focus. Part c) of Figure 4.10 shows the enclosed energy of the measured beams compared with the results taking from the Zemax simulations. Error bars were calculated using the min and max values from the photos captured above. The measured values fall very close to the curve representing the field of view at 200 μm from center. As can be seen from the simulated values at 300 μm from center, the enclosed energy starts to fall off rapidly past 200 μm suggesting that we are very close to the optimal position.

4.7 Summary and Discussion

In this Chapter I have presented my work on the blade trap imaging system. Through careful consideration of our systems efficiencies I have simulated the primary imaging system and found we should be able to achieve high state detection fidelity ($\sim 99.9\%$) with process times comparable with the 11 μs system [23]. After careful alignment of the objective and doublet system, I was able to get performance comparable to the simulated values at 200 μm from the center. The results in Section 4.6, while promising, suggest we still have some aberrations to correct for in our system. Initial investigations suggest that these small aberrations may be difficult to correct for as the contributions from the

doublet become comparable to those from the objective. There are several aspects of our test setup that suggest our final imaging system may be easier to align.

1. The ions are in a fixed position leading to there being less degrees of freedom when it comes to aligning the objective.

2. The custom objective mount will allow us to be within 1 mm of the re-entrant window which gives a greater chance at finding the optimal distance for which the objective has been designed for.

3. In the blade trap, we will be able to use the blades to help with initial alignment of horizontal tilt by aiming for symmetrical aberrations across the imaged blades. By imaging a set of top and bottom blades, the aberrations from the vertical tilt can also be corrected for to some degree.

4. The system will incorporate the motorized translation stage from Section 3.3.2. These can be used to perform fine scans over the xy-plane to find the center of our imaging system.

5. The blade trap system has been engineered to be more stable than this test setup making small adjustments more precise.

Based on our initial tests and these considerations I am confident we will be able to minimize aberrations in the blade trap imaging system.

Often when aligning high NA optical systems, one would use a very long focal length lens which adds insignificant aberrations for the initial alignment. One issue with this strategy is that it's very difficult to image on a camera as a slight shift in the beams position at the objective (either translation or tilt) can lead to shifts at the intermediate image plane that are larger than the camera's sensor. This means we would have to re-position the camera very often during the initial alignment, which adds a substantial amount of time. In the test setup the doublet was used to create the image at IP1 with a moderate degree of efficacy. To improve on this, the doublet and camera system can be carefully aligned before hand using a simpler setup with reduced aberrations. Locking the camera at the focus and making note of the beams position on the sensor will allow us to quickly position the doublet in the optimal position relative to the objective beam. This also has the advantage that small shifts in the objective position will still fall on the camera's sensor due to the shorter focal length of the doublet (and thus less magnification of the system). Previsions have been made to allow for mounting a cage rod system to the back side of the objective mount. These could potentially be used to reference the doublet

to the objective making initial alignment very quick and robust. Removing this could be a challenge and will likely lead to shifts in the system so for final alignment we will have to separate these to systems. At this stage it will be beneficial to place the doublet on a translation stage to make final alignment more repeatable.

The careful analysis of the effects of optical elements on fidelity in Section 4.5.2 showed that adding a few additional lenses to the system only effected fidelity in the fourth decimal. With this in mind, further optimizations can be done by revisiting the Zemax simulations. As can be seem in Figure 4.10 c), the aberrations grow rapidly as you move to the edge of the fields. From initial tests, a triplet (in place of the doublet) can offer better performance at a larger field of view. If adding a single lens into the system is more robust against aberrations (due to misalignment) it may be beneficial even with the slight loss in PMT detection fidelity. With a better beam profile at IP1, it should be easy to design a system that give more uniform performance across the ion chain on the camera. Since the state detection fidelity on the camera is heavily dependent on confining the light of an ion onto one pixel, the benefits of this strategy will likely outweigh the negatives.

Chapter 5

Conclusion

To perform quantum experiments on trapped ions requires many systems to work in unison. Vacuum systems provide isolation from the surroundings, RF is needed to trap the ions and give control over light, lasers manipulate internal energy states and a lab provides a stable environment for all these systems to coexist. As our quantum simulations become more complex the demand on these systems increases. If we do not design and build in robustness to every aspect of a trapped ion system we will have no hope in reaching their full potential. In this thesis I have covered my contributions to designing and building robust systems for our current and future trapped ion quantum simulator. Our DC power distribution system now provides clean, ground referenced voltages to use around the lab to power our electronics without the introduction of excess ground loops. The amplifier box provides stable amplification of RF signals with a compact design while reducing the heat load of our labs environmental system. It also has tested the ability of 3D printed plastic to act as an electrical insulator to prevent the RF signals picking up noise from or transferring noise to the building ground. Motorizing the translation stages in the four-rod 355 nm system has greatly improved our quality of life and provides a repeatability when aligning sensitive optics. By building on the initial design I was able to achieve roughly 70 nm of resolution on all three axes of a Newport translation stage. This ability, along with careful alignment of the optics in the 355 nm paths has lead to ability to reliably perform entangling between our ions and achieve multiple MS flops with minimal decay. This has allowed us to run a multitude of quantum simulations such as many-body spin cooling [1] and has verified the recent results for a novel way to produce xy-type spin interactions with trapped ions [19].

By reducing the out-gassing of the Shapal blade trap holder I increased ion life times by reducing the background collision rate. I was able to achieve our goals of sustaining



Figure 5.1: **Current status of the new lab in B221A.** The 2.5 ft and 5 ft optics tables for the lasers and blade trap system respectively have been place into position. The optics table enclosure frame is mostly installed and is halted until the construction of the air vents is complete.

XHV, reaching 9×10^{-13} mbar vacuum pressures while the blade holder was installed in the blade trap vacuum chamber. To support the next generation trapped ion system a new lab space has been designed to provide a stable, robust environment for the systems mentioned above. Figure 5.1 show the current status of this space under construction with the 2.5 ft and 5 ft optics tables in place and the enclosures partially assembled. We are currently on track to complete the construction of this lab space just in time for the blade trap which is in the final stages of internal assembly. To usher in the new era of trapped ion quantum simulator, an imaging system has been designed for our blade trap. A layout of all the required systems using the side objective has been made with provisions to be modular for future expansion. Simulations of the blade trap's primary imaging system show that high fidelity state detection ($\sim 99.9\%$) with dual PMT's should be possible with detection times of about 25 μs. Using Zemax I have designed a lens system to image the ions onto a camera with minimal aberrations while preserving as many photons as possible. With mechanical stability and optical engineering, the blade trap imaging aims to achieve high fidelity in-situ mid-circuit measurements that will unlock previously unattainable physics. Investigations show that background scattering will be the deciding factor to the viability of performing mid-circuit measurements, and steps have been made to engineer systems to prevent such events from taking place. Initial tests suggest that reaching our simulated values can and will be obtainable with some careful planning.

In the 21st century it's hard to imagine a time when computers did just work, and when an error does occur, it often catches us by surprise. There would however have been a time when modifying the traces of a mother board was not uncommon and further back, when

the early vacuum tube transistors needed to be delicately turned to function correctly. This is the point where many of our quantum simulators are now, and it makes performing complicated experiments a difficult adventure. As we continue to develop robust systems, our quantum simulators become more reliable allowing us to inch ever closer to the full potential of these platforms.

References

[1] Sainath Motlakunta. *Developing a Large-Scale, Programmable Trapped Ion Quantum Simulator with In Situ Mid-Circuit Measurement and Reset*. PhD thesis, University of Waterloo, 2023.

[2] I. M. Georgescu, S. Ashhab, and Franco Nori. Quantum simulation. *Rev. Mod. Phys.*, 86:153–185, Mar 2014.

[3] Brian Skinner, Jonathan Ruhman, and Adam Nahum. Measurement-induced phase transitions in the dynamics of entanglement. *Phys. Rev. X*, 9:031009, Jul 2019.

[4] C. Monroe, W. C. Campbell, L.-M. Duan, Z.-X. Gong, A. V. Gorshkov, P. W. Hess, R. Islam, K. Kim, N. M. Linke, G. Pagano, P. Richerme, C. Senko, and N. Y. Yao. Programmable quantum simulations of spin systems with trapped ions. *Rev. Mod. Phys.*, 93:025001, Apr 2021.

[5] S. Crain, E. Mount, S. Baek, and J. Kim. Individual addressing of trapped 171Yb+ ion qubits using a microelectromechanical systems-based beam steering system. *Applied Physics Letters*, 105(18):181115, 11 2014.

[6] Stefanie Czischek, Giacomo Torlai, Sayonee Ray, Rajibul Islam, and Roger G. Melko. Simulating a measurement-induced phase transition for trapped-ion circuits. *Phys. Rev. A*, 104:062405, Dec 2021.

[7] Wolfgang Paul. Electromagnetic traps for charged and neutral particles. *Rev. Mod. Phys.*, 62:531–540, Jul 1990.

[8] Steven Matthew Olmschenk. *Quantum Teleportation Between Distant Matter Qubits*. PhD thesis, University of Michigan, 2009.

[9] Nikhil Kotibhaskar, Noah Greenberg, Sainath Motlakunta, Chung-You Shih, and Rajibul Islam. Fast and high-yield fabrication of axially symmetric ion-trap needle electrodes via two step electrochemical etching. *Review of Scientific Instruments*, 94(3):033201, 03 2023.

[10] Chung-You Shih, Sainath Motlakunta, Nikhil Kotibhaskar, Manas Sajjan, Roland Hablützel, and Rajibul Islam. Reprogrammable and high-precision holographic optical addressing of trapped ions for scalable quantum control. *npj Quantum Information*, 7(1):57, 12 2021.

[11] Klaus Mølmer and Anders Sørensen. Multiparticle entanglement of hot trapped ions. *Phys. Rev. Lett.*, 82:1835–1838, Mar 1999.

[12] Sainath Motlakunta, Nikhil Kotibhaskar, Chung-You Shih, Anthony Vogliano, Darian Mclaren, Lewis Hahn, Jingwen Zhu, Roland Hablützel, and Rajibul Islam. Preserving a qubit during adjacent measurements at a few micrometers distance. *arXiv preprint arXiv:2306.03075*, 2023.

[13] Raghavendra Srinivas, Emanuel Knill, Robert Sutherland, Alexander Kwiatkowski, Hannah Knaack, Scott Glancy, David Wineland, Shaun Burd, Dietrich Leibfried, Andrew C. Wilson, David Allcock, and Daniel Slichter. High-fidelity laser-free universal control of trapped ion qubits. *Nature*, 597, 2021-09-08 04:09:00 2021.

[14] Jonathan Albert Mizrahi. *Ultrafast Control of Spin and Motion in Trapped Ions*. PhD thesis, University of Maryland, 2013.

[15] Rajibul Islam. *Quantum Simulation of Interacting Spin Models with Trapped Ions*. PhD thesis, University of Maryland, 2012.

[16] Patrick Michael Becker. *Non-Integrable Dynamics in a Trapped-Ion Quantum Simulator*. PhD thesis, University of Maryland, 2021.

[17] Anthony Vogliano. Coherent interactions and thermometry in a trapped ion quantum simulator . Master's thesis, University of Waterloo, 2022.

[18] N B Delone and Vladimir P Krainov. Ac stark shift of atomic energy levels. *Physics-Uspekhi*, 42(7):669, jul 1999.

[19] Nikhil Kotibhaskar, Sainath Motlakunta, Chung-You Shih, Anthony Vogliano, Lewis Hahn, Yu-Ting Chen, and Rajibul Islam. Programmable xy-type couplings through parallel spin-dependent forces on the same trapped ion motional modes. *arXiv preprint arXiv:2307.04922*, 2023.

[20] Volker Hauer Katharina Battes, Christian Day. Outgassing behavior of different high-temperature resistant polymers. *Journal of Vacuum Science and Technology A*, 36:021602, 3 2018.

[21] Katharina Battes, Christian Day, and V. Hauer. Systematic study of the outgassing behavior of different ceramic materials. *Journal of Vacuum Science and Technology B*, 39:034202, 05 2021.

[22] Rachel M. Noek. *Integration of Advanced Optics for Trapped Ion Quantum Information Processing*. PhD thesis, Duke University, 2013.

[23] Stephen Crain, Clinton Cahall, Geert Vrijsen, Emma E. Wollman, Matthew D. Shaw, Varun B. Verma, Sae Woo Nam, and Jungsang Kim. High-speed low-crosstalk detection of a 171Yb+ qubit using superconducting nanowire single photon detectors. *Communications Physics*, 2(1):97, 12 2019.

[24] D. J. Berkeland and M. G. Boshier. Destabilization of dark states and optical spectroscopy in zeeman-degenerate atomic systems. *Phys. Rev. A*, 65:033413, Feb 2002.

[25] Mark Acton. *Detection and Control of Individual Trapped Ions and Neutral Atoms*. PhD thesis, The University of Michigan, 2008.

[26] Stephen G. Crain. *Integrated System Technologies for Modular Trapped Ion Quantum Information Processing*. PhD thesis, Duke University, 2016.

[27] Nikhil Kotibhaskar. Design and construction of an ion trapping apparatus for quantum simulation experiments. Master's thesis, University of Waterloo, 2019.

[28] Sainath Motlakunta. Developing theoretical and experimental tools for a hybrid quantum simulator based on trapped ions. Master's thesis, University of Waterloo, 2018.

[29] Chung-You Shih. Holographic Optical Manipulation of Trapped Ions for Quantum Simulation. Master's thesis, University of Waterloo, 2019.

[30] Chung-You Shih. *Programmable Individual Addressing and Floquet Hamiltonian Dynamics in a Trapped Ion Quantum Processor*. PhD thesis, University of Waterloo, 2023.